Modeling the smoky troposphere of the southeast Atlantic: a comparison to ORACLES airborne observations from September of 2016

Yohei Shinozuka[1,2], Pablo E. Saide[3], Gonzalo A. Ferrada[4], Sharon P. Burton[5], Richard Ferrare[5], Sarah J. Doherty[6,7], Hamish Gordon[8], Karla Longo[1], Marc Mallet[9], Yan Feng[10], Qiaoqiao Wang[11], Yafang Cheng[12], Amie Dobracki[13], Steffen Freitag[14], Steven G. Howell[14], Samuel LeBlanc[2,15], Connor Flynn[16], Michal Segal-Rosenhaimer[2,15], Kristina Pistone[2,15], James R. Podolske[2], Eric J. Stith[15], Joseph Ryan Bennett[15], Gregory R. Carmichael[4], Arlindo da Silva[17], Ravi Govindaraju[18], Ruby Leung[16], Yang Zhang[19], Leonhard Pfister[2], Ju-Mee Ryoo[2,15], Jens Redemann[20], Robert Wood[7] and Paquita Zuidema[13]

[1] Universities Space Research Association, Columbia, Maryland, USA

[2] NASA Ames Research Center, Moffett Field, California, USA

[3] Department of Atmospheric and Oceanic Sciences, and Institute of the Environment and Sustainability, University of California, Los Angeles, California, USA

[4] Center for Global and Regional Environmental Research, The University of Iowa, Iowa City, Iowa, USA

[5] NASA Langley Research Center, Hampton, Virginia, USA

[6] Joint Institute for the Study of the Atmosphere and Ocean, Seattle, Washington, USA

[7] Department of Atmospheric Science, University of Washington, Seattle, Washington, USA

[8] School of Earth & Environment, University of Leeds, LS2 9JT, United Kingdom

[9] CNRM, Météo-France and CNRS, UMR 3589, Toulouse, France

[10] Environmental Science Division, Argonne National Laboratory, Argonne, Illinois, USA

[11] Center for Air Pollution and Climate Change Research (APCC), Institute for Environmental and Climate Research, Jinan University, 510632 Guangzhou, China

[12] Minerva Research Group, Max Planck Institute for Chemistry, 55128 Mainz, Germany

[13] Rosenstiel School of Marine and Atmospheric Science, University of Miami, Miami, Florida, USA

[14] University of Hawaii at Manoa, Honolulu, Hawaii, USA

[15] Bay Area Environmental Research Institute, Moffett Field, California, USA

[16] Pacific Northwest National Laboratory, Richland, Washington, USA

[17] NASA Goddard Space Flight Center, Greenbelt, Maryland, USA

[18] Science Systems and Applications, Inc, Greenbelt, Maryland, USA

[19] Department of Marine, Earth and Atmospheric Sciences, North Carolina State University, Raleigh, North Carolina, USA

[20] School of Meteorology, The University of Oklahoma, Norman, Oklahoma, USA

Correspondence to: Y. Shinozuka (Yohei.Shinozuka@nasa.gov) and P. Zuidema (pzuidema@miami.edu)

Abstract

The southeast Atlantic is home to well-defined smoke outflow from Africa coinciding vertically with extensive marine boundary-layer cloud decks, both reaching their climatological maxima in spatial extent around September. A framework is put forth for evaluating the performance of a range of global and regional aerosol models against observations made during the NASA ORACLES (ObseRvations of Aerosols above CLouds and their intEractionS) airborne mission in September 2016. The sparse airborne observations are first aggregated into 2° grid boxes and into three vertical layers: the cloud-topped marine boundary layer (MBL), the layer from cloud

top to 3 km, and the 3-6 km layer. Aerosol extensive properties simulated for the entire study region for all September suggest that the 2016 ORACLES observations are reasonably representative of the regional monthly average, with systematic deviations of 30% or less. All six models typically place the bottom of the smoke layer at lower altitudes than do the airborne lidar observations by 300-1400 m, whereas model aerosol top heights are within 0-500 m of the observations. All but one of the models that report carbonaceous aerosol masses underestimate the ratio of particulate extinction to the masses, a proxy for mass extinction efficiency, in 3-6 km. Notable findings on individual models include that WRF-CAM5 predicts the mass of black carbon and organic aerosols with minor (~10% or less) biases. GEOS-5 overestimates the carbonaceous particle masses in the MBL by a factor of 3-6. Extinction coefficients in the free troposphere (FT) and above-cloud aerosol optical depth (ACAOD) are 10-30% lower in WRF-CAM5, 30-50% lower in GEOS-5, 10-40% higher in GEOS-Chem, 10-20% higher in EAM-E3SM except for the practically unbiased 3-6 km extinction, and 20-70% lower in the Unified Model, than the airborne in situ, lidar and sunphotometer measurements. ALADIN-Climate also underestimates the ACAOD, by 30%. GEOS-5 and GEOS-Chem predict carbon monoxide in the MBL with small (10% or less) negative biases, despite their overestimates of carbonaceous aerosol masses. Overall, this study highlights a new approach to utilizing airborne aerosol measurements for model diagnosis.

1.   Introduction

The combined radiative impact of shortwave-absorbing aerosol and its interactions with clouds, microphysical and radiative, are subject to large uncertainties over the southeast Atlantic (Myhre et al., 2013; Stier et al., 2013). Efforts to distinguish aerosol effects from meteorology using satellite and reanalysis data suggest that large radiative impacts can be attributed to the shortwave-absorbing aerosol (Adebiyi and Zuidema, 2018; Chand et al., 2009), but ultimately models are necessary for attributing radiative impacts to the underlying processes. Recent modeling studies have emphasized both the radiative impact of aerosol-cloud microphysical

interactions (Lu et al., 2018) and the effects of free-tropospheric stabilization by smoke (Gordon et al., 2018; Sakaeda et al., 2011). The model process uncertainty, to some extent, reflects the paucity of in situ measurements of aerosol properties in this complex region, in which aerosols and clouds typically occur in the same vertical column but are not necessarily co-located. The southeast Atlantic atmosphere has been known to include elevated levels of biomass-burning aerosol (BBA) since at least Fishman et al. (1991), with subsequent satellite studies documenting the spatial extent and optical depth of the BBA more extensively. These confirm that the southeast Atlantic contains a global maximum of BBA present over a bright surface (the underlying stratocumulus deck) (Waquet et al., 2013), resulting in a strong regional climate warming (de Graaf et al., 2014; Peers et al., 2015) that is currently not represented in large-scale models (Stier et al., 2013; Zuidema et al., 2016).

An analysis of surface-based sunphotometer data from Ascension Island (Koch et al., 2009) and a more extensive evaluation using space-based lidar data (Das et al., 2017), conclude that global aerosol models underestimate the amount of BBA brought by long-range transport over the Atlantic. More recent limited in situ aircraft observations on black carbon (BC) mass concentrations further confirm the model underestimate of BC over the remote southeast Atlantic (Katich et al., 2018). Katich et al. (2018) compare these observations to a suite of models assembled by the Aerosol Comparisons between Observations and Models (AEROCOM) project, an international initiative encouraging the rigorous comparison of models to observations by imposing standardizations, such as a single fire emissions inventory, that allow for more fruitful attribution of model differences.

The Das et al. (2017) and Katich et al. (2018) comparisons were against global aerosol models at their developmental stage in 2012 (Myhre et al., 2013). As aerosol models become more sophisticated, more parameterizations are being developed that relate aerosol optical properties to their composition and evolution with time. The aerosol optical properties, primarily the single scattering albedo (SSA) and the vertical structure of extinction, are critical determinants of the direct and semi-direct aerosol radiative effects. To date, with the exception of Katich et al. (2018),

no assessments have been made of the model optical and compositional properties over the smoky southeast Atlantic. This primarily reflects the paucity of in situ measurements over the southeast Atlantic. The South African Regional Science Initiative (SAFARI) in 2000-2001 provided important data sets but these were confined to the vicinity of the south African coast (Swap et al., 2003). These measurements also preceded organized international efforts to evaluate global aerosol models systematically.

Motivated in part by the desire to improve model representation of BBA over the southeast Atlantic, a series of field campaigns initiated in the United States, United Kingdom, France and South Africa have gathered aircraft- and surface-based in situ and remotely-sensed data sets in this climatically important region, beginning in 2016 (Zuidema et al., 2016; Redemann, et al., in preparation). The first deployment of the NASA ObseRvations of Aerosols above CLouds and their intEractionS (ORACLES) campaign took place in September of 2016. The month of September was chosen a priori because this month was thought to reflect the climatological maximum in the spatial extent of overlap of absorbing aerosols above the semi-permanent subtropical southeastern Atlantic stratocumulus deck within the annual cycle, based on satellite passive remote sensing (Adebiyi et al., 2015). Of the two deployed planes, the NASA P3 was instrumented primarily with in situ instruments and flew in the lower- to mid-troposphere. The NASA ER2 flew at about 20 km altitude with downward-viewing remote sensors. Examples of their new insights include a multi-instrument assessment of SSA (Pistone et al., 2019) and the above-cloud aerosol optical depths (ACAOD) (LeBlanc et al., 2019).

An important decision made prior to the deployments was to devote approximately half of all the research flights to routine flights along a pre-established path. The value of unbiased in situ sampling is highlighted in Reddington et al. (2017) as part of the Global Aerosol Synthesis and Science Project. The approach of devoting flight hours specifically to routine flight plans, to facilitate model assessment was arguably first applied during the VOCALS (VAMOS Ocean-Cloud-Atmosphere-Land Study) experiment in the southeast Pacific (Wood et al., 2011; Wyant et al., 2010, 2015). The aircraft campaigns over the southeast Atlantic differ in that a larger altitude

range (up to 6 km) was sampled than during VOCALS, which focused largely on the cloudy boundary layer (Wood et al., 2011). Approximately half of the fifteen ORACLES 2016 flights sampled the truly remote southeast Atlantic directly above the heart of the major stratocumulus deck (Fig. 1; Klein and Hartmann (1993)). Other flights acquired more detailed characterization of the atmospheric vertical structure at the expense of a longer range, and tended to occur closer to the African coast. Data sets from these flights also contribute to this study.

This paper compares modeled aerosol products with ORACLES 2016 observations. Our study extends more deeply into evaluating the composition, size, and optical properties of the modeled smoke particles above the southeast Atlantic than has been possible to date (described further in Section 2.1). The six models participating in this exercise all strive to represent the smoky southeast Atlantic atmosphere (Mallet et al., 2019) and are either versions of the aerosol transport models used for in-field aerosol forecasts or global and regional models applied for assessing the climate impact of the smoke (Section 2.2). Spatiotemporal ranges surrounding the ORACLES flights are chosen to address data sampling challenges (Section 3). The extent to which the sampled data represent the climatological monthly-mean is assessed in Section 4. The model-observation comparisons along the flights begin with the smoke plume altitude (Section 5). Aerosol properties are then compared within fixed altitude ranges (Section 6). The findings common among the models and divergent ones are discussed (Section 7). A summary is provided in Section 8.

2. Observations and Models

2.1. Observations

The instruments and the observed/derived values are described in detail in the Appendix, with general descriptions provided here and summarized in Table 1. BC, a key smoke component strongly absorbing of shortwave absorption, is measured by the Single Particle Soot Photometer (SP2; see Section 9.1.1) and organic and sulfate aerosol masses by a time-of-flight aerosol mass

spectrometer (AMS; Section 9.1.2). Aerosol size affects both the optical and the cloud-nucleating properties of BBA. Particles with dry diameters between 60-1000 nm are measured with an ultra-high sensitivity aerosol spectrometer (UHSAS; Section 9.1.3). This allows us to determine the volumetric arithmetic mean diameter of the accumulation mode, the cube root of the volume-to-number ratio after the volume is divided by $\pi/6$.

In situ aerosol scattering is measured by a nephelometer, and aerosol absorption by a particle soot absorption photometer (PSAP), both at an instrument relative humidity (RH) that is typically below 40% (Section 9.1.4). From these measurements, extinction coefficient and SSA at 530 nm as well as scattering and absorption Ångström exponents (SAE, AAE) across 450-700 nm are derived. A detailed comparison of the SSA values to those from other instruments is shown in Pistone et al., (2019).

Statistics of the aerosol intensive properties (SSA, AE, volumetric mean diameter and an extinction-to-mass ratio) are only calculated from individual measurements with the midvisible dry extinctions greater than 10 Mm^{-1}, thereby reducing the noise apparent at lower aerosol concentrations.

The NASA Langley Research Center High Spectral Resolution Lidar (HSRL-2; Section 9.1.5), deployed from the ER2 during 2016, provides measurements of the aerosol extinction vertical profiles at 355 and 532 nm. The HSRL-2 employs the HSRL technique (Shipley et al., 1983) to measure calibrated, unattenuated backscatter and aerosol extinction profiles and also has a higher signal-to-noise ratio than the space-based lidars, so it can extensively sample the complete aerosol vertical structure of the aerosol. These mitigate the well-documented low signal-to-noise issue with the space-based CALIOP lidar (Kacenelenbogen et al., 2011; Liu et al., 2015; Lu et al., 2018; Pauly et al., 2019; Rajapakshe et al., 2017). One measure of the ACAOD is derived from the HSRL-2 532-nm measurements. Another is available from 4STAR (Section 9.1.6), a sunphotometer / sky-radiometer (LeBlanc et al., 2019) from the low-flying P3 when above cloud top.

1   We use particulate 532-nm backscattering coefficient and cloud top height, which are

2   among the standard HSRL-2 products (Burton et al., 2012), to define the bottom and top heights

3   of the smoke plumes. We set a threshold particulate backscattering coefficient at 0.25 Mm^{-1}sr^{-1}.

4   For the layer bottom, we do not search within 300 m of the layer top or beneath the cloud top

5   height. Our statistics do not include the cases where the smoke base is identified to be higher than

6   4 km, to avoid artefact noise due to imperfectly cleared cirrus. The extinction threshold is

7   approximately equivalent to an extinction of 15 Mm^{-1} for an estimated extinction-to-backscattering

8   ratio of 60 sr and to a BC mass concentration of 200 ng m^{-3} at standard temperature and pressure

9   (STP, 273K and 1013 hPa) For model output we use this BC value as the smoke plume threshold,

10   as this property is inherent to biomass burning and because the models do not produce

11   backscattering (the lidar backscattering method does not distinguish between smoke and other

12   aerosols such as marine aerosol). These are conservative choices emphasizing the clear presence

13   of smoke (57% of the 60s-average SP2 measurements in the free troposphere (FT) exceed 200 ng

14   m^{-3} STP). Though not explored in the current analysis, the subjective choice will affect the gap

15   distance between the smoke plume bottom and the cloud top.

16   Carbon monoxide (CO), a tracer for air masses originating from combustion, is measured

17   by a Los Gatos Research CO/CO2/H2O Analyzer (Section 9.1.7). Overall these variables are

18   selected because they are robustly-observed, are pertinent to the absorption of shortwave

19   radiation and are available in most models. Cloud condensation nuclei number concentrations,

20   organic carbon (a derived quantity from the AMS measurements) and cloud properties are not

21   compared in this study.

22   2.2.   Models

23   The six assessed models are summarized in Table 2 and detailed in the Appendix. The

24   models are assessed using their native parameterizations and emission inventories, with no

25   standardization applied across the models, in contrast to the planned experiments of the

26   AEROCOM initiative. The primary ORACLES aerosol forecast tools are a version of the regional

WRF-CAM5 model (Section 9.2.1) possessing simpler aerosol microphysics (WRF-AAM, WRF with aerosol-aware microphysics (Diamond et al., 2018; Saide et al., 2016)) and the NASA GEOS-5 global aerosol model (Section 9.2.2). Additional analysis is performed with these two models to assess whether the in situ data from the flight days are representative of the monthly-mean distributions more typical of Intergovernmental Panel on Climate Change studies. The WRF-CAM5 model is also the only model containing all of the aerosol variables with complementary aircraft measurements.

The UK Unified Model (UM; Section 9.2.5) in its numerical weather prediction configuration produced forecasts for the CLARIFY campaign in 2017, with simpler smoke aerosol emissions and microphysics than that assessed within the current study. The three other state-of-the-art models are GEOS-Chem (Section 9.2.3), EAM-E3SM (Section 9.2.4) and the ALADIN-Climate (Section 9.2.6; also assessed within Mallet et al. (2019)).

A threshold of 200 ng m^{-3} of BC mass concentration at STP is used to locate the model smoke plumes. The only exception is ALADIN-Climate, for which an extinction threshold of 17 Mm^{-1} is used. As with the observations, the model intensive properties are only aggregated using data with 550 nm extinctions (under dry conditions if reported otherwise under the ambient humidity) greater than 10 Mm^{-1}. The volume mean diameter is computed from the accumulation mode only, as smaller aerosol sizes contribute little to the overall aerosol number and mass.

3.   Framework for the Model-Observation Comparison

3.1.   Vertical Ranges

The analysis is performed in three altitude ranges: the cloud-topped marine boundary layer (MBL), the region above the cloud top up to 3 km, and from 3 to 6 km. During September 2016, within the sampled domains, the cloudy boundary layer is materially separated from the much drier FT by a strong inversion, evident in aircraft RH profiles (Fig. 2). For the in situ observations available from the P3, we define the MBL as altitudes below (RH(%) - 60)*40 m. This definition

1   is useful in that it does not require a vertical gradient, which is only available for limited flight

2   segments.

3   For models, the basic definition of the MBL top height is the level where the vertical

4   derivative of the specific humidity with respect to altitude is a minimum. The basic concept is to

5   define the depth of the layer where the surface has significant immediate influence on the moisture.

6   This depth is often larger than the traditional "well-mixed" region where the potential temperature

7   is nearly constant. To take into account differences in boundary layer dynamics between land and

8   ocean, and between the northern (latitude north of $5°S$) and southern regions, we implement some

9   modifications to this basic scheme. First, we calculate dq/dz, where q is specific humidity and z is

10   altitude, at all grid points up to the level D. Here D is 3 km over oceanic regions and 6 km over

11   land (small islands in the SE Atlantic, e.g., St Helena and Ascension, are considered oceanic).

12   Next, we find the altitude z_0 where dq/dz is a minimum. The different altitudes D for land and

13   ocean are chosen because: (1) boundary layers (even the well-mixed convective boundary layer)

14   on the African continent are often quite deep, up to 5 km; and (2) occasionally the dq/dz minimum

15   over the oceans is at the top of the smoke layer (so we restrict the MBL depth to a maximum of 3

16   km). For our model sampling of the MBL, we use data from the surface up to half the height of

17   the MBL to avoid the possibility of cloud artifacts.

18   The two definitions of the cloud-topped MBL differ only slightly within the WRF-CAM5

19   model, in which the RH-based definition places the top of the MBL 120 m higher than the gradient-

20   based one, in the mean. An interest in facilitating future model-observation intercomparisons form

21   2017 and 2018 aircraft data taken in more equatorward regions of the southeastern Atlantic, where

22   cloud cover is lower and clouds are more multi-layered, justifies the use of the two MBL height

23   definitions.

24   For both observations and models, the altitude of 3 km is chosen to distinguish the lower

25   and mid FT. The lower FT, up to 3 km, contains aerosols that are more likely to mix into the MBL

26   over the southeastern Atlantic at some future time (Diamond et al., 2018). In contrast, the only

27   interaction of aerosols in the upper 3-6 km layer with the underlying cloud deck is through

radiation. Note that for the lower FT, we require that the ambient RH be below 60% and the altitude at least 500 m, to exclude the observations in the MBL. HSRL-2 observations generally show a better defined plume with larger aerosol loads in the mid FT than in the lower FT, the latter often separated from the cloud top (Burton et al., 2018).

3.2. Horizontal and Temporal Ranges

An additional challenge for any model evaluation using observations, especially in situ, is the scale mismatch. The in situ measurements are collected at spatial scales of approximately one sample per ∼100 m, one location at a time. In contrast, the model values represent averages over a horizontal grid spacing of tens of kilometers, available at regular intervals. The sampling bias is dealt with by aggregating the data from both the observations and models into 2°-by-2° latitude-longitude boxes and slightly larger ones (Fig. 3). Box-whisker plots summarize the full range of the distribution through reporting the 10th, 25th, 50th (the median), 75th and 90th percentiles as well as the means and standard deviations. This approach is similar to that applied within AEROCOM studies (Katich et al., 2018) but the data aggregation occurs within smaller domains and aims to capture regional spatial gradients, similar to Wyant et al. (2010, 2015).

Observations are first averaged over one minute from their native values, to limit the small-scale variability and instrumental noise. A one-minute mean is equivalent to an approximate horizontal scale of 7-10 km at the typical P3 aircraft speed and 12 km at the typical ER2 speed.

One of the three main corridors encompasses the routine flight track, with individual grid boxes centered at $(14^o E, 24^o S)$, $(12^o E, 22^o S)$, $(10^o E, 20^o S)$, $(8^o E, 18^o S)$, $(6^o E, 16^o S)$, $(4^o E, 14^o S)$, $(2^o E, 12^o S)$ and $(0^o E, 10^o S)$, each having corners at 2° north, east, south and west, respectively, of the center. Another, coastal north-south corridor has the southernmost grid box centered on 22° S, spanning between $9^o E$ and $11.75^o E$. Seven grid boxes are located every 2° north of this, with the northernmost grid box centered on $8^o S$. A third, west-east corridor covers the larger domain of the ER2 measurements, with individual grid boxes spanning latitudinally between $10^o S$ and 6° S and separated longitudinally at 2° intervals beginning at $3^o W$ to the west and $13^o E$ in the east.

The box for St. Helena Island spans between 6.72º W and 4.72º W, between 16.93º S and 14.93º S.

All P3 and ER2 flights occurred during daytime, with data primarily gathered between 9 am to 4 pm in Central Africa Time (7 am to 2 pm UTC). The P3 sampled for 96 hours in the diagonal and meridional corridors. The ER2 sampled for 30 hours in these domains and 8 hours in the zonal corridor. The models are sampled at the three-hourly times closest to those of the measurements, except for the climatology study presented in Section 4. Diurnal variations in aerosol properties are small and not considered.

4.   Representativeness of the Airborne Sampling

An a priori analysis based on MODIS clear-sky aerosol optical depths indicates that the ORACLES sampling is sufficient to capture the monthly mean. A posteriori analysis based on WRF-CAM5 and GEOS-5 model output of aerosol extinctions, presented below, confirms this. The daytime model outputs for the whole month of September occurring within the defined grid boxes are compared to the smaller data set of model output sampled closest in space and time to the observations.

The WRF-CAM5 model aerosol extinctions between 3-6 km altitudes corresponding to the days when the HSRL-2 extinctions are available (Fig. 4a, blue boxes and whiskers) generally agree well with the values based on the entire month (black boxes and whiskers). The same can be said for the comparison based on the P3 flight days (Fig. 4b). This is true for both the diagonal and meridional corridors (left and right halves, respectively, of each panel). This conclusion is based on an evaluation of the mean bias (MB) and the root-mean-square deviations (RMSD) for the two model populations. The MB between the monthly-mean and flight-day-only means is between -10 % and +10 % of the monthly means. The RMSD based on the model output from the flight days only are 20-30 % of the monthly-mean values for each aircraft. The MB and RMSD values are provided in Table 3 for the two aircraft and three layers. The MBL (Fig. 4d) MB and RMSD values are similar to those for 3-6 km. In the layer extending above MBL up to 3 km (Fig. 4c), the

means of the extinction modeled along the P3 flight tracks exceed the monthly means on the diagonal corridor and at the southern half of the meridional corridor, by approximately 20 % across the boxes. Comparisons based on BC, organic aerosol (OA), CO and ACAOD are mostly similar to those based on the light extinction. The only exception occurs within the MBL, wherein the mean BC and OA mass concentrations on flight days exceed the monthly-mean values by approximately 30-40 % (Table 3). In-flight sampling decisions favoring more smoky conditions may be responsible for this bias.

This analysis is used to assess if the observations gathered on flight days are representative of the monthly-mean spatial trends across the southeast Atlantic, at the different vertical levels. The FT of the southern end of the sampled domain is less smoky in the mean than the northern end (LeBlanc et al., 2019), the latter being closer to the main smoke outflow of the region at ~10° S. The flight days capture the spatial trend well in the mid troposphere and MBL, and somewhat less so in the lower FT especially near the coast.

Results from GEOS-5 for the in situ properties for 3-6 km and MBL and the ACAOD are similar to those from WRF-CAM5 in terms of the climatology representativeness. The magnitude of the MB in 3-6 km is slightly smaller, at 5 % or less (Table 3). For the lower FT (above MBL-3 km), GEOS-5 shows that ORACLES flights sampled lighter aerosol loading than the month-long average, by about 10 %, while WRF-CAM5 shows heavier smoke loads as mentioned above. The discrepancy between the two models is related to the way each model identifies the smoke bottom height. While GEOS-5 sees little systematic difference (+100 m) for the ORACLES flights compared to the climatology, in WRF-CAM5 the smoke bottom height was about 400 m higher, on average (Table 3).

To summarize, comparisons between the aerosol loadings within the WRF-CAM5 and GEOS-5 simulations from flight-days-only to those from the full month suggest that the MBL aerosol loading sampled during the 2016 ORACLES flights likely exceeded monthly-mean values. WRF-CAM5 and GEOS-5 disagree as to whether the lower FT had heavier or lighter aerosol loadings on flight days than the monthly-mean. We note, however, that the mean biases are

1 generally between -10 % and +30 % in the lower FT and MBL, and less within the 3-6 km layer.

2 To this extent the ORACLES observations, at least in the diagonal and meridional corridors,

3 represent the regional climatology for September 2016.

4 **5.   Evaluation of Model Aerosol Plume Heights**

5 An initial evaluation of the free-tropospheric aerosol layer top and bottom altitudes

6 prepares for the comparisons carried out for the comparison layers. The HSRL-2 observations

7 indicate that smoke layer top is highest, 5-6 km, between 9-17°S (Fig. 5a). The mean aerosol bases

8 are typically located at 1.5-2.5 km rising slightly from north to south. The observed plume top and

9 bottom heights show little zonal gradient along 8°S (Fig. 5b): 1740 ± 290 m for the bottom and

10 5250 ± 180 m for the top, the value after the $\pm$ symbol expressing the standard deviation among

11 the mean altitudes of the 2° grid boxes between 3°W and 13°E.

12 All of the models tend to place the smoke plume at a lower altitude than the HSRL-2,

13 especially in the northern half of the area. GEOS-5 and GEOS-Chem underestimate the mean top

14 heights most severely, with an MB of -500 m for both. The negative bias does not exceed 200 m

15 for UM, EAM-E3SM, WRF-CAM5 and ALADIN-Climate (Fig. 5, Table 3). These biases are less

16 than the model vertical resolution at these altitudes (e.g., WRF-CAM5 has ~500 m layer thickness

17 at 5 km altitude) so that at least the <200m underestimates are within the expected model

18 uncertainty.

19 The underestimates in the aerosol layer bottom heights are more diverse (300-1400 m)

20 among the models. The MB is more negative than for the top height for each of the models, i.e.,

21 all models generally overestimate the smoke plume vertical thickness. As with the top heights, the

22 GEOS-Chem and GEOS-5 models underestimate the bottom altitudes most severely.

23 Despite generally placing the FT aerosol layers too low, most models are able to capture

24 an equatorward increase in the aerosol layer tops, and an opposite gradient in the layer bases. Most

25 models skilfully locate the maximum aerosol layer tops at 13-15°S close to the coast (the

26 meridional corridor). One exception is ALADIN-Climate, which overall underestimates the top

height by ~500 m but overestimates further to the south. As a result, while the bias is small, the variability between the grid boxes is somewhat greater (RMSD 800 m) than for WRF-CAM5 (400 m), UM (400 m) and EAM-E3SM (500 m) and is closer to that for GEOS-5 (600 m) and GEOS-Chem (800 m).

The variability is generally predicted too low within the southernmost boxes. The observed smoke heights near 20° S are more variable than further north, possibly related to more complex (re)circulation patterns away from the primary jet outflow core. The models have more difficulty representing this variability and do not necessarily capture the spatial trends in the smoke heights.

6.   Evaluation of Models at Bulk Vertical Levels

The six models are compared against the observations within the three pre-defined bulk vertical layers using box-whisker plots to capture the mean and the variability. Comparisons for the diagonal corridor are shown to the left of the meridional one in Figs. 6-14. The mean bias and standard deviations of each of the model products from the observations are summarized in Table 4. The model products provided in this section are sampled near the location and time of the airborne measurements, not monthly values

6.1.   Aerosol Chemical and Physical Properties

Fig. 6 compares the observed versus modeled BC mass concentrations at the ambient temperature and pressure for the five reporting models. In the mid FT (3-6 km altitude; Fig. 6a), the WRF-CAM5 model (blue color) is in the best agreement with the SP2 observations (black), with an RMSD between the 16 grid box means of 170 ng m^{-3}. The agreement of the GEOS-5 (orange) model with the measurements is slightly poorer, with an RMSD of 210 ng m^{-3}. These values are around 30 % of the mean observed values, as noted in parentheses in Table 4. Little systematic bias is discernible in the figure. The MB of the box means is as small as +10 % (Table 4).

In contrast, GEOS-Chem has practically zero MB but an RMSD that is 50 % of the mean (Fig. 6, green) due to underestimates in the northern half of the diagonal corridor (NW-SE boxes) away from the land (the left half of the panel) and overestimates nearer the coast (the right half). This shift is consistent with the increasing underestimate in the smoke top height as the plume advects towards the west in this model (Fig. 4). UM and EAM-E3SM underestimate BC mass concentrations in the 3-6 km layer by 40-50 % in all regions, with this systematic bias driving the RMSD.

Above the MBL up to 3 km (Fig. 6b), the models typically underestimate the BC loading further offshore and to the north, and agree better with the observations towards the south, where less smoke is present. The strong observed gradient from south to north is not represented in most models. The model-observation RMSD is greater in the lower FT than in the mid FT for WRF-CAM5 (60 %), GEOS-5 (60 %) and EAM-E3SM (80 %). GEOS-Chem performs in this layer similar to its performance in the 3-6 km layer, with an RMSD of 50 % and no apparent bias. UM underestimates less severely in this layer (-20 % MB) than in 3-6 km.

Much less BC is observed in the MBL (Fig. 6c) than in the FT. GEOS-5 overestimates MBL BC, more significantly (+160 % MB) than in the FT (+10-20 %), as does GEOS-Chem. EAM-E3SM shows better agreement with observations in the MBL than above it. WRF-CAM5 and UM do not noticeably skew the BC vertical distribution towards the MBL. WRF-CAM5 overestimates in the northernmost boxes on the diagonal corridor, but by less than GEOS-5 does.

Measured organic aerosol (OA) mass concentrations at the ambient temperature and pressure, shown in Fig. 7, increase from south to north near the coast, with concentrations lower further offshore. The models capture this trend, but show somewhat greater deviations in OA than in BC. The RMSD in the 3-6 km layer, for example, is around 40 % for WRF-CAM5, 90 % for GEOS-5, 60 % for GEOS-Chem, 100 % for EAM-E3SM and 50 % for UM.

In the lower FT the GEOS-5 OA is more than twice that observed, and in the MBL more than six times. The biases are more positive in the MBL than in the FT in all models. For both BC and OA, the RMSD is also greater at lower altitudes.

Only two models (WRF-CAM5 and the UM) report an aerosol diameter. The diameter of the emitted aerosol is prescribed within these models, and allowed to evolve thereafter. The measured volumetric mean dry aerosol diameters from the UHSAS are close to 200 nm, with little geographical or altitude variation.

The UM volumetric mean diameter is greater than the observation by 60-70 nm in the FT. The modeled diameters are 20 % greater in the ambient RH. In the MBL the UM-observation differences in diameter are marginally smaller, especially on the diagonal corridor. WRF-CAM5 volumetric mean aerosol diameters, which are calculated for the dry conditions, exceed measured values by 40-80 nm in the FT and by 100 nm in the MBL (Fig. 8). The cause is a prescribed volumetric geometric mean diameter of 375 nm for the emitted accumulation mode particles (the geometric standard deviation is 1.8). Future simulations will use diameters closer to that representative of biomass burning emissions.

6.2.   Aerosol Optical Properties

Fig. 9 shows model-derived ACAOD compared to observed mid-visible wavelength values from the ER2-borne lidar and the P3-borne sunphotometer. The WRF-CAM5 ACAOD values are biased low, by 10-20 % (Fig. 9, Table 4), particularly in the northern region closer to the plume core. Underestimates by GEOS-5 and ALADIN-Climate are larger still (~30-40 %) and EAM-E3SM overestimates by 20 %. While these models show similar degrees of deviations for the two instruments, GEOS-Chem overestimates by 40 % for the HSRL-2 but only by 5 % for 4STAR.

Model differences from the observed mid-visible light extinction (Fig. 10) broadly follow those for ACAOD. The top panel shows lidar-derived extinction at ambient RH, while the other three panels show the sum of nephelometer scattering and PSAP absorption coefficients measured at low (~20 %) RH. For both comparisons the model values refer to ambient RH. In the FT, the ambient-RH/dry ratio of light scattering is estimated to be less than 1.2 for the 90 % of the time when the dry scattering exceeds 1 Mm^{-1}, according to concurrent, once-per-second measurements with two nephelometers with instrument RH set respectively to high (~80 %) and low (~20 %). In

contrast, in the MBL, where the relative humidity typically exceeds 85 % and the aerosols are more hygroscopic, the effect of aerosol hygroscopic swelling on the extinction is pronounced, exceeding 2.2 for half of our measurements. Thus, while the WRF-CAM5 extinctions are systematically lower (by 30 %) relative to the in situ values in both mid FT and MBL, the underestimate in extinction within the MBL is in practice more severe. Since the WRF-CAM5 model predicts RH with little bias, the severe underestimate may be due to poor representation of the aerosol properties within the MBL. The comparison to the HSRL-2 ambient extinction only shows a 20 % underestimate. This could be due to the sampling bias in the in situ observation, although the differences in the locations and sampling time between the two aircraft preclude a definitive conclusion.

GEOS-5 underestimates the FT extinction to a greater degree than does WRF-CAM5, by 30-50 %, but grossly overestimates extinction within the MBL. GEOS-Chem shows biases to the positive direction in the MBL (+130 %) and in the FT (by 10-30 %). EAM-E3SM indicates smaller overestimates (~10 % or smaller in magnitude) in the FT, with values in the northern half of the near-coast corridor particularly close to the observation. The overestimate in the MBL by EAM-E3SM is even more severe than that by GEOS-5. UM generally underestimates the extinction, by 30 % compared to the lidar extinction on the ambient humidity basis and by 40-80 % compared to the in situ extinction on the dry basis.

The Ångström exponent of scattering is another, independent if indirect measure of particle size that is more readily available from the models included here than is the aerosol size itself. The Ångström exponent is computed as the slope of a linear fit of the scattering versus wavelength on logarithmic scales for cases where the 550 nm extinction exceeds 10 Mm^{-1}. Large Ångström exponents tend to correspond to smaller particle sizes. The scattering Ångström exponent is systematically underestimated by WRF-CAM5, by an absolute value of 0.6-0.8 (Fig. 11), consistent with the overestimated aerosol mean sizes (Fig. 8). UM, GEOS-5 and GEOS-Chem agree better with the observed values in the FT, with an RMSD of 0.1. The largest deviations are found in the northern end of the near-coast flights where the observations are relatively sparse.

1 Within the MBL, all of the models tend to underestimate the scattering Ångström exponent,
2 indicating model particle sizes that are larger than observed.

3   The absorption Ångström exponent differs from the scattering Ångström exponent in that
4 it is primarily a function of particle composition, and secondarily of particle size. In the FT the
5 absorption Ångström exponent is systematically underestimated by 0.1 in the UM for dry aerosols,
6 by 0.4-0.5 in WRF-CAM5, GEOS-5 and GEOS-Chem (Fig. 12). The modelled flatter spectra may
7 reflect model overestimates in BC absorption or underestimates in absorbing organic material or
8 dust. The models have very small ranges in the absorption Ångström exponent, both within each
9 of the comparison boxes and across them.

10   SSA is key to establishing the radiative impact of the aerosol layer. The dry in situ
11 observations indicate midvisible SSA values of 0.85 to 0.89 in the mid FT and 0.80 to 0.86 in the
12 lower FT. SSA in the lower FT (Fig. 13b) is simulated by WRF-CAM5 and GEOS-5 well, with
13 minor biases (+0.01 or smaller) and RMSD of 0.01-0.02. In the mid FT (Fig. 13a), WRF-CAM5
14 systematically underestimates SSA by 0.03. GEOS-5 also underestimates it, but by noticeably
15 smaller margins near the coast. GEOS-Chem overestimates SSA most severely, by 0.07-0.08 in
16 both layers. EAM-E3SM also overestimates by 0.08 in the lower FT, by 0.02 in the mid FT.
17 However, all of these models diagnose SSA in ambient conditions, while the observations are in
18 dry conditions. The UM predicts both, and while the ambient simulated SSA also agrees
19 reasonably well with the dry observations, the SSA for dried particles in the FT is underestimated
20 by 0.07 in mid FT and 0.03 in lower FT. The models generally overestimate SSA in the MBL (Fig.
21 13c), but this assessment is subject to particularly poor statistics due to the scarcity of cases with
22 dry extinction exceeding 10 Mm^{-1} and the lack of adjustment for the humidity effect.

23   **6.3.   Carbon Monoxide**

24   We also compare CO mixing ratio from the three models reporting it to measured quantities
25 (Fig. 14). The measurements range from 60 ppbv to over 500 ppbv. The three models tend to
26 underestimate, especially further offshore in 3-6 km and in the northern half of the near-coast

1 corridor. WRF-CAM5 systematically underestimates by ~20 % in the FT, as does GEOS-5 to a

2 lesser degree (~10 %), with GEOS-Chem somewhere in between. In the MBL, where the observed

3 mixing ratio is typically below 130 ppbv, the models also typically predict low, most notably near

4 the southern end and near the coast. GEOS-Chem shows an altitude dependence in MB (-20 % in

5 3-6 km, -5 % below), but the dependence is not as strong as that seen in the carbonaceous masses.

6 The relative RMSD, at 20-30 % for these models, is smaller than for any of the aerosol extensive

7 properties.

8 **7. Discussion**

9 The six models in this study have several common features, most notably the underestimate

10 of the smoke bottom height. The models diverge widely on other properties, such as the magnitude

11 of carbonaceous aerosol masses and light extinction. Here we discuss the results with respect to

12 the model representations of the smoke emission, transport and mass extinction efficiency.

13 The low biases of smoke heights are a consequence of skewed aerosol mass vertical

14 profiles. As the heights are determined with BC in all models but one, the model that most severely

15 overestimates the masses (both BC and OA) in the MBL, GEOS-5, most severely underestimates

16 the smoke height. The model that underestimates the height least severely, WRF-CAM5 (setting

17 aside ALADIN-Climate which does not produce the masses), overestimates the MBL masses least

18 severely. Another manifestation of the difficulty in representing the plume base is the generally

19 greater random deviations, expressed as RMSD, in the carbonaceous masses at lower FT and MBL.

20 The low bias of the smoke layer heights has previously been attributed to an overestimate

21 of the subsidence over the ocean (Das et al., 2017), an underestimate in the smoke injection heights

22 at the source (Myhre et al., 2003) and the dry deposition velocity scale factor (Regayre et al.,

23 2018). Of these, an exaggerated subsidence over the ocean would not only influence the transport

24 of smoke but also the top height of clouds. Often the smoke base height is determined by the cloud

25 top height in models, as smoke concentrations in the MBL are usually below the threshold used

26 for defining the smoke boundaries. If models underestimate cloud top heights for stratocumulus

1   decks, as they often do in the southeast Pacific (Wyant et al., 2015), that could contribute to the

2   smoke bottom underestimates and diversity. But it is not clear whether subsidence fully explains

3   the underestimates by as large as 1400 m.

4   Neither do subsidence and injection heights explain another common feature in the present

5   study: the three models that provide CO neither dramatically overestimate it in the MBL nor skew

6   its vertical distribution towards lower layers relative to the observations. This is internally

7   consistent for WRF-CAM5 where the altitude dependence is also small for OA and virtually non-

8   existent for BC. For GEOS-5 and GEOS-Chem the altitude dependence is strikingly different

9   between the carbonaceous aerosol masses and CO.

10   Fig. 15a-c illustrate this disconnection on a pre-aggregation basis (i.e., 60s means). BC and

11   CO are compared on logarithmic scales in order to show the entire range of values including low

12   CO cases common in the MBL. The logarithmic scales and the use of geometric mean and standard

13   deviation later in the discussion also handle the ratios (of aerosol masses to CO) better, by keeping

14   the average ratio and the ratio of averages identical to each other.

15   The observed relationship (Fig. 15a) is tight for CO above 130 ppb. Most of these data

16   points occur in the FT (grey dots). Most MBL observations (blue) show CO between 60-130 ppbv.

17   In this range the relationship with BC is less tight, probably because smoke, upon entering MBL

18   clouds, loses aerosols to wet scavenging. BC is lower than 500 ng m^{-3} in the MBL in almost all

19   cases, and is often as small as 10 ng m^{-3}. WRF-CAM5 shows a similar BC-CO relationship (Fig.

20   15b). The only notable deviation from the observations is in the somewhat smaller diversity in

21   carbonaceous aerosol masses, evident as a function of the CO (Fig. 15) and by location (box-

22   whiskers in Fig. 6 and 7).

23   GEOS-5 (Fig. 15c, note the fewer data points due to the larger grid boxes), on the other

24   hand, has high BC values in the MBL with values exceeding 100 ng m^{-3} in most cases with

25   excursions up to 1000 ng m^{-3}. The relationship between OA and CO is qualitatively similar (Fig.

26   15f). The somewhat higher scatter of the data points suggests that the degrees of secondary

1 condensation and chemical aging processes vary significantly, since OA is subject to these

2 processes whereas BC is not.

3   If the degrees of mixing of smoke into the MBL were the only source of error, the aerosol

4 masses and CO would be biased by similar proportions. The combinations of these two variables

5 would be on or near the observed relationships. But they are not, as the figure shows. Additional

6 factors must drive GEOS-5 (and GEOS-Chem) to produce anomalously high BC, but not CO. The

7 only process that is known to significantly affect CO, removal through oxidation and cloud uptake,

8 is negligible on the timescale of advection (a few days to two weeks) from the African biomass

9 burning regions. Spatiotemporal sampling bias, positive and small (+20 % relative to the regional

10 September average (Section 4)), does not explain the BC overestimates by a factor of 3.

11   With these possibilities excluded, we expect that processes influencing aerosols in an

12 altitude-dependent manner but not CO must be the primary reason. Aerosol removal processes

13 may be misrepresented, although Das et al. (2017) found that those in GEOS-5 contributed little

14 to the differences they observed. Other possible explanations are secondary formation, coagulation

15 and condensation.

16   EAM-E3SM and UM generally underestimate the BC masses in the FT. While model

17 uncertainty in representing aerosol removal and transport cannot be excluded, the most likely cause

18 is an overall underestimate of the smoke aerosol mass. In particular, in EAM-E3SM, monthly

19 biomass burning emissions for an average year, mean of 1997-2000, are used, which dampen the

20 model's ability to faithfully reproduce episodic burning events. Low emissions could also arise

21 from the insensitivity of satellite retrievals to very small fires (Fornacca et al., 2017; Petrenko et

22 al., 2017; Zhu et al., 2017).

23   For OA, factors other than emission seem to be at play. The altitude of OA is biased low

24 in all models, more significantly than that of the less hygroscopic BC. Assuming negligible

25 systematic biases in the observations, this may be due to insufficient wet removal in the model

26 MBL. Consistently, the EAM-E3SM also puts significantly more sulfate (relative to the

27 observations) towards the MBL, although WRF-CAM5 and UM do not. Another possible

explanation is in the representation of SOA. In the UM all monoterpene emissions are at the surface with no representation of plumes, and the lifetime of SOA may be too short for it to be elevated. EAM-E3SM includes a slower yield-based SOA formation from six gaseous precursors (Liu et al., 2012), but the SOA formation in the southeast Atlantic has not been evaluated.

The extinction coefficient in the FT and ACAOD within GEOS-5 and WRF-CAM5 are, counterintuitively, underestimated while the masses are generally overestimated. This is partly because some aerosol components beyond BC, OA and sulfate are not incorporated into the models. WRF-CAM5, for example, does not compute nitrate and ammonium, which contribute 9% and 5%, respectively, to the total aerosol mass as observed with the AMS and SP2.

Nevertheless, the missing aerosol mass components are too small to fully account for the extinction underestimates. Sampling measurement bias is unlikely to fully explain the discrepancy, because the modeled extinction is also biased by -10% against the better-vertically-sampled HSRL-2 observations whose higher abundance reduces sampling bias (ER2 flights without HSRL-2 measurements are excluded from our study). We therefore conclude that the mass extinction efficiency (MEE) implicit in these models must be underestimated.

While the missing mass components prevent us from computing MEE in the models, the ratio of extinction to carbonaceous masses (OA+BC) can illustrate its spatial and inter-model variabilities in an approximate manner, provided that biomass-burning particles dominate the aerosol mass and extinction (which is the case in the biomass-burning plume in the FT). The quasi-MEE calculated from the box mean ambient extinction and masses in the FT is shown in Fig. 16. Each model takes a fairly constant value across the locations. In the lower FT, WRF-CAM5, GEOS-Chem, EAM-E3SM have values near 8 m^2g^{-1}. UM Ambient has 6 m^2g^{-1}.

In 3-6 km, the modeled quasi-MEE values show wider inter-model spreads. While WRF-CAM5 and GEOS-Chem have 8-10 m^2g^{-1}, EAM-E3SM and UM Ambient indicate values closer to 6 m^2g^{-1}. The latter are smaller than the observed dry values, which are 8 m^2g^{-1} or greater in almost all boxes. GEOS-5 underestimates it most severely in both layers.

The underestimates are more pronounced when humidification is taken into consideration. The aerosol swelling from moisture within the FT contributes 20% or less to the measured extinction. In contrast, UM, which provides both dry and ambient extinction, sees humidification by around 50% (compare UM Dry and UM Ambient in Fig. 16). WRF-CAM5 also has a large humidification factor, although the dry values are not shown in Fig. 16. On a dry, pre-aggregation basis (Fig. 15), the geometric mean for cases with the combined mass exceeding 10 μgm^{-3} is 2.0 m^{2}g^{-1} for WRF-CAM5, compared with 8.5 m^{2}g^{-1} for the dry observation (Fig. 15g) and 1.2 m^{2}g^{-1} for GEOS-5 (Fig. 15i).

While the observations may have systematic biases such as underestimates in the OA masses, it is unlikely that they are large enough to explain the model-observation discrepancies in quasi-MEE. Mie calculations for common ranges of refractive index and density find that MEE for the observed UHSAS size distributions cannot be much smaller than 4 m^{2}g^{-1}; the quasi-MEE should be greater than this. The underestimates by some of the models are counterintuitive. With the volumetric mean diameter around 200 nm and overestimated, and with scattering Ångström exponent underestimated, the MEE and quasi-MEE are expected to be overestimated.

Furthermore, the pre-aggregation values of quasi-MEE (Fig. 15) in the two FT layers are less diverse with the observations (the geometric standard deviation is 1.4) than with the models (2.4 and 1.8, respectively). WRF-CAM5 evidently has three distinct values for the smoke, regardless of the day of flight. What little variations the observed relationships have depend somewhat on the flight day in a way that is not reproduced by the two models.

These results reveal the difficulty in representing both aerosol extinction and mass correctly. MEE serves as either the very cause of such limitation or a test of realism, depending on whether a model estimates the two aerosol properties independently from each other or not. If it does, then the model representation of aerosol mixing states, size, and refractive indices, as well as ambient RH matters.

So far we have discussed the means and their biases. Our data also allow discussion of the random deviations between the models and observations, expressed by the RMSD of the box

means over the corridors. They are significantly greater than the magnitude of systematic biases for most extensive properties. Also, within any of the boxes there is no clear correspondence between the modeled and observed variabilities.

These are partly a result of counting statistics. Disagreement is found when just a few minutes of data are available for in-plume measurements in a given comparison gridbox. For example, the near-coast boxes at 8° S in the FT layers have only 4-5 minutes of data. Also, some of the observations represent a small fraction of the flight hours. For example, 4STAR provides relatively sporadic sampling of ACAOD, as the aircraft needed to be located right above clouds.

The variability can also be attributed to model specifications. GEOS-Chem generally exhibits greater variability, both within boxes and across them, than WRF-CAM5. This is most noticeable in ACAOD. Since these two models employ the same daily emission scheme and allocate it to diurnal cycle representative of daytime burning in similar manners, the difference in the variability must be due to other aerosol processes and model resolution.

For the intensive optical properties, the variability in the modeled values is typically much smaller than the observed variability. As an exception, EAM-E3SM's SSA values vary more widely than do the observations within each box in the lower FT. But they significantly overestimate the observations, possibly because of weak emissions of absorbing smoke particles in this model. SSA variability is a topic addressed in accompanying papers (Pistone et al., 2019; Doherty et al., in preparation).

8. Summary

We have compared six model representations of biomass-burning smoke and other aerosols against the 130-hour airborne observations made over the southeast Atlantic in September 2016. The major findings are:

- All six models underestimate the smoke base height. GEOS-5 and GEOS-Chem do so most severely, by 1400 m and 900 m respectively. The two models significantly overestimate the OA and BC masses, but not CO mixing ratio, in the MBL.

- GEOS-5, EAM-E3SM, UM and WRF-CAM5 underestimate the ratio of light extinction to carbonaceous masses in 3-6 km altitude. While the OA mass is generally overestimated, extinction coefficient in the FT is biased low by some models.

- The aerosol loads sampled in ORACLES 2016 are generally between -10% and +30% of the regional September average, according to WRF-CAM5 and GEOS-5.

1   **9.   Appendix**

2   **9.1.   Observations**

3   **9.1.1.   SP2**

4   A Single Particle Soot Photometer (SP2) was deployed to measure the mass of individual

5   refractory BC (rBC) particles by heating them to incandescence when passing a powerful laser

6   beam (Schwarz et al., 2006; Stephens et al., 2003). The peak value of this incandescence signal

7   has been shown to linearly correlate with the mass of the rBC particle (Stephens et al., 2003). The

8   unit was calibrated for various rBC masses with Fullerene soot (Alfaa Aesar, Lot #F12S011) using

9   Fullerene effective density estimates from Gysel et al. (2011). Assuming a density of 1.8 g cm^{-3}

10   for airborne rBC mass measurements the detection limit of the 4-channel instrument was in the

11   range of 55-524 nm mass-equivalent diameter (MED). Overall, uncertainty of the SP2 mass

12   measurements due to laser power and pressure fluctuations as well as detection limits has been

13   estimated to 25% (Schwarz et al., 2006), while rBC concentration losses are expected to be small

14   since much of the ambient BC number concentration is found within the detection limits of the

15   SP2 (Schwarz et al., 2010).

16   **9.1.2.   AMS**

17   Bulk submicron non-refractory aerosol composition (~ 50 to 500 nm vacuum aerodynamic

18   diameter) was provided by the Time of Flight (ToF) – Aerodyne aerosol mass spectrometer (AMS)

19   in form of organic mass (ORG), sulfate (SO4), nitrate (NO3), and ammonium (NH4) (DeCarlo et

20   al., 2008). The AMS sampled at a rate of ~1.38 cm^{3}s^{-1}, and used an aerodynamic lens at constant

21   pressure (600 hPa) to focus 35 nm - 500 nm non refractory particles onto the 600°C heated surface

22   under high vacuum ~10^{-5} Pa. The particles are then evaporated off the heated surface, and ionized

23   by 70 eV electron impaction. The aerosol then passes through a mechanical chopper operating at

24   100 - 150 Hz, which alternately blocks and unblocks the particle beam. Lastly, the particles are

25   carried through the flight chamber chemically analyzed by the Time of Flight Mass Spectrometer

(ToF-MS). The AMS was generally operated in the high sensitivity V-mode to facilitate constant measurements during flights. The accuracy of these measurements was estimated to 50% with 10% precision during ORACLES. A more thorough description of the University of Hawaii AMS and data processing techniques using data analysis toolkit SQUIRREL v.1.57l and PIKA v.1.16l can be found elsewhere (Shank et al., 2012; Sueper, 2018)

9.1.3. UHSAS

Particle size distributions from 60 to 1000 nm were measured with a Ultra-High Sensitivity Aerosol Spectrometer (Droplet Measurement Technologies, Boulder CO, USA). It uses scattered light from a 1054 nm laser to determine particle size. The long wavelength suppresses the ambiguity due to Mie scattering, though the highly absorbing nature of the ORACLES aerosol may result in substantial undersizing of particles > 300 nm. It was calibrated with monodisperse polystyrene latex spheres. The inlet system included a 400ºC thermal denuder that could be switched in and out to identify the refractory fraction of the aerosol, though those data are not presented here. The inlet system had significant losses, particularly for particles <80nm.

9.1.4. Nephelometer and PSAP

Total and submicrometer aerosol light scattering were measured onboard the aircraft using two TSI model 3563 3-λ nephelometers (at 450, 550, and 700 nm) corrected according to Anderson and Ogren (1998). Light absorption coefficients (at 470, 530 and 660 nm) were measured using two Radiance Research particle soot absorption photometers (PSAP's). The PSAP absorption corrections were performed according to an updated algorithm (Virkkula, 2010), however levels of instrument noise remain 0.5 Mm^{-1} for a 240–300 s sample average, comparable to values reported previously (Anderson et al., 2003; McNaughton et al., 2011). The SSA at 530 nm was calculated from the scattering and absorption measurements, after adjusting the absorption coefficients to the wavelength by linear regression on the log-log space.

9.1.5. High spectral resolution lidar (HSRL-2)

The NASA Langley 2nd generation airborne High Spectral Resolution Lidar (HSRL-2) was deployed on board the ER2 and made remote-sensing measurements below the aircraft of vertically resolved aerosol extinction coefficient (355 nm, 532 nm), aerosol backscattering coefficient (355, 532, 1064 nm) and aerosol depolarization (355, 532, 1064 nm). Other products include AOD, AOD above cloud, lidar ratio (extinction to backscatter ratio), Ångström exponent, and a qualitative aerosol type mask (Burton et al., 2012). AOD, extinction and backscatter are measured using the HSRL technique (Shipley et al., 1983), which is implemented using an iodine filter at 532 nm (Hair et al., 2008) and an interferometer at 355 nm (Burton et al., 2018). Vertical resolutions are 315 m for extinction, lidar ratio, and extinction Ångström exponent; and 15 m for backscatter, particle depolarization ratio, and backscatter-related Ångström exponent. Horizontal resolution is 10 seconds for backscatter and depolarization or about 2 km at a typical ER2 cruise speed. For extinction and AOD, the horizontal resolution is one minute or about 12 km. Note that during ORACLES 2017 and 2018 HSRL-2 was deployed from the NASA P3 aircraft. Further details about the instrument, calibration, and uncertainty can be found in Hair et al. (2008), Rogers et al. (2009) and Burton et al. (2018).

9.1.6. Airborne Sunphotometer (4STAR)

Aerosol Optical Depth (AOD) is measured from the solar direct beam's attenuation using the Spectrometers for Sky-Scanning Sun-Tracking Atmospheric Research (4STAR) (Dunagan et al., 2013) integrated on board the NASA P3 aircraft. Using 2 spectrometers, 4STAR samples light with wavelengths ranging from 350 nm to 1750 nm, with sampling resolution of 0.2 - 1 nm below 1000 nm and 3 - 6 nm at longer wavelengths. The full width of the field of view for the direct beam irradiance measurement is 2.4° with radiometric deviations of less than 1% across this span. 4STAR is calibrated pre- and post- deployment using the Langley extrapolation method at the Mauna Loa Observatory, in addition to comparing AOD measured during high altitude flight segments to stratospheric aerosol. The relative standard deviation of all these calibrations is 0.83%

(1.12%) at 500 nm (1040 nm). After calibration errors, corrections for window deposition, instability in tracking, and internal throughput variations, the average uncertainty for 4STAR during ORACLES 2016 for the AC-AOD is 0.011 (0.013) at 501 nm (1020 nm) (LeBlanc et al., 2019)

9.1.7. Carbon monoxide

CO was measured with a gas-phase $CO/CO_2/H_2O$ Analyzer (ABB/Los Gatos Research $CO/CO_2/H_2O$ Analyzer (907-0029)), modified for flight operations. It uses off-Axis ICOS technology to make stable cavity enhanced absorption measurements of CO, CO_2, and H_2O in the infrared spectral region, technology that previously flew on other airborne research platforms with a precision of 0.5 ppbv over 10 seconds (Liu et al., 2017; Provencal et al., 2005)

9.2. Models

Refer to Table 2 for a summary, including model resolution.

9.2.1. WRF-CAM5

WRF-CAM5 is a version of the WRF-Chem model that is coupled with the Community Atmosphere Model version 5 (CAM5) physics package, as implemented by (Ma et al., 2014). The CAM5 physics suite includes the deep convection scheme of Zhang and McFarlane (1995), the shallow cumulus scheme (Bretherton and Park, 2009), the University of Washington turbulence parameterization (Bretherton and Park, 2009), the Morrison and Gettelman (2008) two-moment microphysics scheme, a simplified macrophysics scheme (Neale et al., 2010), and a modal aerosol module with three modes (Aitken, Accumulation, and Coarse) (MAM3) (Liu et al., 2012) coupled with the gas phase chemistry of Carbon Bond Mechanism version Z (Zaveri and Peters, 1999). All aerosol species within each mode is assumed to be internally mixed and mass by species and total number concentrations are tracked. Aerosol optical properties are computed using the WRF-Chem routines (Fast et al., 2006) by converting MAM3 modes into eight sectional size bins (39 nm to 10 μm) followed by Mie theory calculation. Organic aerosol and black carbon refractive indices are

assumed to be 1.45+0i (e.g, no brown carbon considered) and 1.85+0.71i constant across shortwave radiation. Cloud droplet activation is represented by Fountoukis and Nenes (2005) as implemented by Zhang et al. (2015) into WRF-CAM5 for giant CCN, CCN from insoluble particles such as black carbon and dust particles. The effect of convective entrainment on aerosol activation (Barahona and Nenes, 2007) is only applied to convective clouds. The Zhang and McFarlane deep convection scheme has been modified by Lim et al. (2014) following Song and Zhang (2011) to include a two-moment cloud microphysics parameterization for convective clouds. Hence aerosol effects on clouds and precipitation are represented for both convective and non-convective clouds in WRF-CAM5. Daily smoke emissions are from the Quick Fire Emission Data set version 2 (QFED2) (Darmenov and da Silva, 2013) and a diurnal cycle representative of daytime burning is applied. The model was initialized every 5 days from the NCEP Final Operational Global Analysis (FNL) on a 1 by 1 degree grid, and CAMS reanalysis, with the first 3 days of simulations considered as model spin-up and not used in our analysis.

9.2.2. GEOS-5

The Goddard Earth Observing System version 5, is a global modeling system developed at NASA Global Modeling and Assimilation Office (GMAO)(Molod et al., 2015; Rienecker et al., 2008). It is a state-of-art modeling tool used for near-real time weather and air quality forecasts. It also serves as tool for climate variability studies and reanalysis for research (MERRA-2)(Randles et al., 2017). GEOS-5 includes modules for solving atmospheric circulation and composition, chemistry, ocean circulation and land surface processes. Furthermore, GEOS-5 uses a robust atmospheric data assimilation system using the Grid-point Statistical Interpolation (GSI) algorithm, which includes AOD assimilation from MODIS (Terra and Aqua), among others. Aerosols are treated online using GOCART (Goddard Chemistry Aerosol Radiation and Transport) (Chin et al., 2002; Colarco et al., 2010). Black and organic carbon aerosols are treated separately, with organic carbon aerosols represented as a function of the particulate organic matter (POM), with POM = 1.4 * organic carbon mass (Textor et al., 2006). The single-moment mass is

1 converted to an extinction using a black carbon mass extinction efficiency of 10.7 m^{2}g^{-1} and 5.83

2 m^{2}g^{-1} for POM, both at 550 nm (Colarco et al., 2010). The carbonaceous aerosols are coupled with

3 the radiation module. QFED2 is used as daily input of biomass burning emissions. For this study,

4 GEOS-5 used initial conditions from its reanalysis product (MERRA-2), with a resolution of

5 around 25 km (0.25°x0.31° latitude x longitude grid) with 72 vertical levels (hybrid-sigma) from

6 the surface

9.2.3. GEOS-Chem

8   GEOS-Chem version 12.0.0 (http://www.geos-chem.org/) is a global 3-D model of

9 atmospheric composition driven by assimilated meteorological data GEOS-FP data (Lucchesi,

10 2013) from the Global Modeling and Assimilation Office (GMAO) at NASA Goddard Space

11 Flight Center. The GEOS-FP data have 1-hourly and 3-hourly temporal resolution, 72 vertical

12 layers, and 0.25x0.3125° horizontal resolution. The original horizontal resolution is then degraded

13 to 2° x2.5° for the input to GEOS-Chem. Aerosol types simulated in GEOS-Chem include sulfate–

14 nitrate–ammonium aerosols, carbonaceous aerosols, sea salt, and mineral dust. The simulation of

15 carbonaceous aerosols was originally described by Park et al. (2003). Daily smoke emissions have

16 been updated to the Quick Fire Emission Data set version 2 (QFED2) (Darmenov and da Silva,

17 2015) and a diurnal cycle representative of daytime burning is applied. Dry deposition in GEOS-

18 Chem follows a stand resistance-in-series scheme (Wesely, 1989), accounting for gravitational

19 settling and turbulent dry transfer of particles to the surface (Zhang et al., 2001). Wet deposition

20 in GEOS-Chem includes scavenging in convective updrafts, as well as in-cloud and below-cloud

21 scavenging from convective and large-scale precipitation (Liu et al., 2001), and distinguish the

22 difference between snow/ice scavenging and rain scavenging (Wang et al., 2011, 2014). Aerosol

23 optical depth are calculated online using Mie theory, assuming lognormal distribution of externally

24 mixed aerosols after accounting for hygroscopic growth. The optical properties used in the

25 calculation are based on the Global Aerosol Data Set (GADS) data (Koepke et al., 1997), with

1 modifications in size distribution (Drury et al., 2010; Jaeglé et al., 2011; Wang, 2003a, 2003b),

2 and hygroscopic growth factors (Jimenez et al., 2009).

9.2.4. EAM-E3SM

4 The EAM-E3SM is the atmospheric component of the Department of Energy Exascale

5 Energy Earth System Model (E3SM) version 1 (Golaz et al., 2019). It is a global atmospheric

6 model branched off from the CAM 5.3 and updated with the physics similar to changes from

7 CAM5.3 to CAM6 incorporated. The model configuration used in this study includes a spectral

8 element dynamical core at approximately 100 km horizontal resolution and 72 vertical layers. The

9 planetary boundary layer turbulence, shallow convection and cloud macrophysics are treated with

10 a simplified version of the unified parameterization - CLUBB (Cloud Layers Unified By

11 Binormals; Larson and Golaz (2005); Larson (2017)). The EAM-E3SM aerosol module is the four-

12 mode version of the Modal Aerosol Module (MAM4) in the CAM5.3 (Liu et al., 2016). It simulates

13 internally mixed major aerosol compounds (sulfate, BC, primary and secondary organic matter,

14 dust, sea salt and marine organic aerosols), which are distributed into three size modes including

15 Aitken, accumulation, and coarse modes, plus an additional primary carbon mode representing

16 freshly emitted BC and primary organic matter. In each aerosol size mode, mass concentrations of

17 aerosol compounds and a total number concentration of aerosol mixture are calculated at each

18 model time step and evolve in time. Detailed description of EAM physics and model evaluations

19 are given in Rasch et al. (2019) and Xie et al. (2018). For this study, EAM simulations were

20 conducted in the nudging mode with temperature, wind speeds and moisture fields nudged to the

21 ERA-Interim reanalysis data every 6 hours. One-year model simulations are performed after

22 spinning-up the model and model outputs from August to October are used in comparison. Aerosol

23 and cloud properties are output every 3 hours to account for the diurnal variations. Emissions of

24 anthropogenic aerosols are taken from the IPCC-AR5 emissions for circ. year 2000. Biomass

25 burning emissions are based on GFED emissions averaged over 1997 and 2000.

9.2.5.   Unified Model

The Unified Model is the numerical weather prediction and global climate model of the UK Meteorological Office, known also as HadGEM3 in its climate modeling configuration. The model configuration used here is similar to the global model setup used by Gordon et al. (2018), but is now based on GA7.1 with version 11.2 of the model code, while Gordon et al. (2018) used a setup based on GA6.1 with version 10.3. The spatial resolution is N216 (approximately 60x90km at the Equator) and for this study instantaneous diagnostic output at three-hourly intervals was produced. The model sea surface temperatures are fixed from the OSTIA temperature record and the horizontal winds above the boundary layer are nudged to ERA-interim reanalysis. The model run is a continuation of that used for 1-10 August 2016 by Gordon et al. (2018), which was initialized from an operational forecast on 20 July 2016. Aerosols in the model are simulated using the two-moment GLOMAP-mode scheme within the United Kingdom Chemistry and Aerosols framework. There are five log-normal aerosol modes containing sulfate, black and organic carbon, and sea salt components; dust and nitrate are not included. A reduced chemistry scheme for aerosol formation via the sulfur cycle uses oxidants from climatologies. Smoke emissions are read in daily from the FEER inventory for 2016 (Ichoku and Ellison, 2014) as a log-normal mode of aerosol with diameter 120nm; they are distributed vertically within the boundary layer as in Gordon et al. (2018). Other emissions are either calculated by the model, as in the case of sea spray, or taken from the CMIP5 inventories. The single-moment cloud microphysics scheme of Wilson and Ballard (1999) and pc2 sub-grid cloud scheme of Wilson et al (2008) are used. Convection is parameterized where it cannot be resolved. The refractive index of BC and the updraft speeds in the activation scheme now follow GA7.1 prescriptions used in the CMIP6 experiments, while the hygroscopicity of the aerosol constituent components now follows Petters and Kreidenweis (2007), which is another change compared to Gordon et al. (2018).

9.2.6.   ALADIN-Climate

The ALADIN-Climate model is a regional climate model (RCM), which is developed in CNRM/Meteo-France. We use here the version 6 of ALADIN–Climate (Mallet et al., 2019), which has a similar physical package to the global climate model ARPEGE–Climate (Voldoire et al., 2017) used in the CMIP6 exercise. It is a bi-spectral semi-implicit semi-lagrangian model, with a 12 km horizontal resolution. ALADIN-Climate includes the Fouquart and Morcrette radiation scheme (Morcrette, 1989), based on the ECMWF model incorporating effects of greenhouse gases, direct and semi-direct effects of aerosols as well as the first indirect effect of hydrophilic aerosols. The ALADIN-Climate model incorporates a radiative scheme to take into account the direct and semi-direct effects of five aerosol types (sea salt, desert dust, sulfates, black and organic carbon aerosols). Here, a new version of the ALADIN-Climate model, including notably a more detailed treatment (optical and hygroscopic properties, e-folding time) of smoke aerosols, have been used for this specific inter-comparison exercice (Mallet et al., 2019). The ALADIN-Climate simulation has been conducted for three months (August-September-October 2016) englobing the ORACLES period. The model used the ERA-INT reanalyses as lateral boundary conditions. For this simulation, the GFED emissions inventory based on CMIP6 has been used for biomass burning emissions, with scale factors from Petrenko et al. (2017). An important point is that aerosol (SO2, BC and OC) emissions for the year 2014 have been used as this specific year represents the last year of the historical CMIP6 period using realistic BC-OC emissions from biomass-burning (based on GFED inventory). Emissions have been used as the first model level without any considerations about the altitude of injection of smoke particles in this simulation. As detailed in Mallet et al. (2019), this model does not integrate secondary organics and a POM to OC ratio have been used in this simulation, based on Formenti et al. (2003).

Data availability

The P3 and ER2 observational data (NASA Ames Earth Science Project Office, 2017a, 2017b) are available through www.espo.nasa.gov/oracles. The aggregated model and observation products are available at https://espo.nasa.gov/sites/default/files/box_P3ER2Models_2016mmdd_R8.nc .

Author contribution

SPB, RF, AD, SF, SGH, SL, CF, MSR, KP, JRP, EJS, JRB and YS operated instruments during the ORACLES intensive observation periods. PES, GAF, HG, KL, MM, YF, QW, YC, GRC, AdS, RG, RL, YZ delivered model products. LP and JMR developed the methodology of determining MBL height. PES, SJD, JR, RW and PZ formulated the model-observation comparison. YS organized all products and applied statistical techniques. YS, GAF and PZ visualized the results. YS, PZ, PES wrote most of the first draft. YS, PES, GAF, SPB, RF, SJD, HG, MM, YF, SL, MSR, KP, RL, YZ, LP, RW and PZ edited the manuscript. JR, RW and PZ led the efforts to acquire funding for the ORACLES mission. PZ administered and supervised the study.

Competing Interests

The authors declare that they have no conflict of interest.

Acknowledgements

ORACLES is a NASA Earth Venture Suborbital 2 investigation, funded by NASA's Earth Science Division and managed through the Earth System Science Pathfinder Program Office. H

Gordon is funded by the NERC CLARIFY project under grant NE/L013479/1, and acknowledges use of the Monsoon2 system, a collaborative facility supplied under the Joint Weather and Climate Research Programme, a strategic partnership between the UK Met Office and the Natural Environment Research Council. The authors would like to thank Sampa Das for her valuable comments, and Nicolas Bellouin for the code to diagnose dry aerosol optical properties from the Unified Model.

References

Adebiyi, A. A. and Zuidema, P.: Low Cloud Cover Sensitivity to Biomass-Burning Aerosols and Meteorology over the Southeast Atlantic, J. Clim., 31(11), 4329–4346, 2018.

Adebiyi, A. A., Zuidema, P. and Abel, S. J.: The Convolution of Dynamics and Moisture with the Presence of Shortwave Absorbing Aerosols over the Southeast Atlantic, J. Clim., 28(5), 1997–2024, 2015.

Anderson, T. L. and Ogren, J. A.: Determining aerosol radiative properties using the TSI 3563 integrating nephelometer, Aerosol Sci. Technol., 29, 57–69, 1998.

Anderson, T. L., Masonis, S. J., Covert, D. S., Ahlquist, N. C., Howell, S. G., Clarke, A. D. and McNaughton, C. S.: Variability of aerosol optical properties derived from in situ aircraft measurements during ACE-Asia, J. Geophys. Res., 108(D23), 8647, doi:10.1029/2002JD003247, 2003.

Barahona, D. and Nenes, A.: Parameterization of cloud droplet formation in large-scale models: Including effects of entrainment, J. Geophys. Res., 112(D16), 6837, 2007.

Bretherton, C. S. and Park, S.: A New Moist Turbulence Parameterization in the Community Atmosphere Model, J. Clim., 22(12), 3422–3448, 2009.

Burton, S. P., Ferrare, R. A., Hostetler, C. A., Hair, J. W., Rogers, R. R., Obland, M. D., Butler, C. F., Cook, A. L., Harper, D. B. and Froyd, K. D.: Aerosol classification using airborne High Spectral Resolution Lidar measurements – methodology and examples, Atmospheric Measurement Techniques, 5(1), 73–98, 2012.

Burton, S. P., Hostetler, C. A., Cook, A. L., Hair, J. W., Seaman, S. T., Scola, S., Harper, D. B., Smith, J. A., Fenn, M. A., Ferrare, R. A., Saide, P. E., Chemyakin, E. V. and Müller, D.: Calibration of a high spectral resolution lidar using a Michelson interferometer, with data examples from ORACLES, Appl. Opt., 57(21), 6061–6075, 2018.

Chand, D., Wood, R., Anderson, T. L., Satheesh, S. K. and Charlson, R. J.: Satellite-derived direct

1   radiative effect of aerosols dependent on cloud cover, Nat. Geosci., 2, 181, 2009.

2   Chin, M., Ginoux, P., Kinne, S., Torres, O., Holben, B. N., Duncan, B. N., Martin, R. V., Logan, J. A.,
3   Higurashi, A. and Nakajima, T.: Tropospheric Aerosol Optical Thickness from the GOCART Model and
4   Comparisons with Satellite and Sun Photometer Measurements, J. Atmos. Sci., 59(3), 461–483, 2002.

5   Colarco, P., da Silva, A., Chin, M. and Diehl, T.: Online simulations of global aerosol distributions in the
6   NASA GEOS-4 model and comparisons to satellite and ground-based aerosol optical depth, J. Geophys.
7   Res., 115(D14), doi:10.1029/2009jd012820, 2010.

8   Darmenov, A. and da Silva, A.: The Quick Fire Emissions Dataset (QFED) – Documentation of versions
9   2.1, 2.2 and 2.4. NASA Technical Report Series on Global Modeling and Data Assimilation, NASA TM-
10 2013-104606, 32, 183, 2013.

11 Darmenov, A. S. and da Silva, A. M.: The Quick Fire Emissions Dataset (QFED): Documentation of
12 Versions 2.1, 2.2 and 2.4. Volume 38; Technical Report Series on Global Modeling and Data
13 Assimilation, [online] Available from: https://ntrs.nasa.gov/search.jsp?R=20180005253 (Accessed 9 May
14 2019), 2015.

15 Das, S., Harshvardhan, H., Bian, H., Chin, M., Curci, G., Protonotariou, A. P., Mielonen, T., Zhang, K.,
16 Wang, H. and Liu, X.: Biomass burning aerosol transport and vertical distribution over the South African-
17 Atlantic region: Aerosol Transport Over SE Atlantic, J. Geophys. Res. D: Atmos., 122(12), 6391–6415,
18 2017.

19 DeCarlo, P. F., Dunlea, E. J., Kimmel, J. R., Aiken, A. C., Sueper, D., Crounse, J., Wennberg, P. O.,
20 Emmons, L., Shinozuka, Y., Clarke, A., Zhou, J., Tomlinson, J., Collins, D. R., Knapp, D., Weinheimer,
21 A. J., Montzka, D. D., Campos, T. and Jimenez, J. L.: Fast airborne aerosol size and chemistry
22 measurements above Mexico City and Central Mexico during the MILAGRO campaign, Atmos. Chem.
23 Phys., 8(14), 4027–4048, 2008.

24 Diamond, M. S., Dobracki, A., Freitag, S., Small Griswold, J. D., Heikkila, A., Howell, S. G., Kacarab,
25 M. E., Podolske, J. R., Saide, P. E. and Wood, R.: Time-dependent entrainment of smoke presents an
26 observational challenge for assessing aerosol–cloud interactions over the southeast Atlantic Ocean,
27 Atmos. Chem. Phys., 18(19), 14623–14636, 2018.

28 Doherty, S. J., Saide, P., Zuidema, P., Shinozuka, Y., Ferrada, G., Mallet, M., Meyer, K., Painemal, D.,
29 Howell, S. G., Freitag, S., Smirnow, N., Dobracki, A., Podolske, J., Pfister, L., Ueyama, R., Nabat, P.,
30 Wood, R. and Redemann, J.: A summary and model-observation comparison of vertically-resolved
31 aerosol and cloud properties over the Southeast Atlantic, in preparation.

32 Drury, E., Jacob, D. J., Spurr, R. J. D., Wang, J., Shinozuka, Y., Anderson, B. E., Clarke, A. D., Dibb, J.,
33 McNaughton, C. and Weber, R.: Synthesis of satellite (MODIS), aircraft (ICARTT), and surface
34 (IMPROVE, EPA-AQS, AERONET) aerosol observations over eastern North America to improve
35 MODIS aerosol retrievals and constrain surface aerosol concentrations and sources, J. Geophys. Res. D:
36 Atmos., 115(D14) [online] Available from:

https://rmets.onlinelibrary.wiley.com/doi/pdf/10.1029/2009JD012629, 2010.

Dunagan, S. E., Johnson, R., Zavaleta, J., Russell, P. B., Schmid, B., Flynn, C., Redemann, J., Shinozuka, Y., Livingston, J. and Segal-Rosenhaimer, M.: Spectrometer for Sky-Scanning Sun-Tracking Atmospheric Research (4STAR): Instrument Technology, Remote Sensing, 5(8), 3872–3895, 2013.

Fast, J. D., Gustafson, W. I., Jr., Easter, R. C., Zaveri, R. A., Barnard, J. C., Chapman, E. G., Grell, G. A. and Peckham, S. E.: Evolution of ozone, particulates, and aerosol direct radiative forcing in the vicinity of Houston using a fully coupled meteorology-chemistry-aerosol model, J. Geophys. Res., 111(D21), 2981, 2006.

Fishman, J., Fakhruzzaman, K., Cros, B. and Nganga, D.: Identification of widespread pollution in the southern hemisphere deduced from satellite analyses, Science, 252(5013), 1693–1696, 1991.

Formenti, P., Elbert, W., Maenhaut, W., Haywood, J., Osborne, S. and Andreae, M. O.: Inorganic and carbonaceous aerosols during the Southern African Regional Science Initiative (SAFARI 2000) experiment: Chemical characteristics, physical properties, and emission data for smoke from African biomass burning, J. Geophys. Res. D: Atmos., 108(D13) [online] Available from: https://onlinelibrary.wiley.com/doi/abs/10.1029/2002JD002408, 2003.

Fornacca, D., Ren, G. and Xiao, W.: Performance of Three MODIS Fire Products (MCD45A1, MCD64A1, MCD14ML), and ESA Fire_CCI in a Mountainous Area of Northwest Yunnan, China, Characterized by Frequent Small Fires, Remote Sensing, 9(11), 1131, 2017.

Fountoukis, C. and Nenes, A.: Continued development of a cloud droplet formation parameterization for global climate models, J. Geophys. Res., 110(D11), doi:10.1029/2004jd005591, 2005.

Golaz, J., Caldwell, P. M., Van Roekel, L. P., Petersen, M. R., Tang, Q., Wolfe, J. D., Abeshu, G., Anantharaj, V., Asay-Davis, X. S., Bader, D. C., Baldwin, S. A., Bisht, G., Bogenschutz, P. A., Branstetter, M., Brunke, M. A., Brus, S. R., Burrows, S. M., Cameron-Smith, P. J., Donahue, A. S., Deakin, M., Easter, R. C., Evans, K. J., Feng, Y., Flanner, M., Foucar, J. G., Fyke, J. G., Griffin, B. M., Hannay, C., Harrop, B. E., Hoffman, M. J., Hunke, E. C., Jacob, R. L., Jacobsen, D. W., Jeffery, N., Jones, P. W., Keen, N. D., Klein, S. A., Larson, V. E., Leung, L. R., Li, H., Lin, W., Lipscomb, W. H., Ma, P., Mahajan, S., Maltrud, M. E., Mametjanov, A., McClean, J. L., McCoy, R. B., Neale, R. B., Price, S. F., Qian, Y., Rasch, P. J., Reeves Eyre, J. E. J., Riley, W. J., Ringler, T. D., Roberts, A. F., Roesler, E. L., Salinger, A. G., Shaheen, Z., Shi, X., Singh, B., Tang, J., Taylor, M. A., Thornton, P. E., Turner, A. K., Veneziani, M., Wan, H., Wang, H., Wang, S., Williams, D. N., Wolfram, P. J., Worley, P. H., Xie, S., Yang, Y., Yoon, J., Zelinka, M. D., Zender, C. S., Zeng, X., Zhang, C., Zhang, K., Zhang, Y., Zheng, X., Zhou, T. and Zhu, Q.: The DOE E3SM Coupled Model Version 1: Overview and Evaluation at Standard Resolution, J. Adv. Model. Earth Syst., 108, 1, 2019.

Gordon, H., Field, P. R., Abel, S. J., Dalvi, M., Grosvenor, D. P., Hill, A. A., Johnson, B. T., Miltenberger, A. K., Yoshioka, M. and Carslaw, K. S.: Large simulated radiative effects of smoke in the south-east Atlantic, Atmos. Chem. Phys., 18(20), 15261–15289, 2018.

de Graaf, M., Bellouin, N., Tilstra, L. G., Haywood, J. and Stammes, P.: Aerosol direct radiative effect of smoke over clouds over the southeast Atlantic Ocean from 2006 to 2009: DE GRAAF ET AL, Geophys. Res. Lett., 41(21), 7723–7730, 2014.

Gysel, M., Laborde, M., Olfert, J. S., Subramanian, R. and Gröhn, A. J.: Effective density of Aquadag and fullerene soot black carbon reference materials used for SP2 calibration, Atmospheric Measurement Techniques, 4(12), 2851–2858, 2011.

Hair, J. W., Hostetler, C. A., Cook, A. L., Harper, D. B., Ferrare, R. A., Mack, T. L., Welch, W., Izquierdo, L. R. and Hovis, F. E.: Airborne High Spectral Resolution Lidar for profiling aerosol optical properties, Appl. Opt., 47(36), 6734–6752, 2008.

Ichoku, C. and Ellison, L.: Global top-down smoke-aerosol emissions estimation using satellite fire radiative power measurements, Atmos. Chem. Phys., 14(13), 6643–6667, 2014.

Jaeglé, L., Quinn, P. K., Bates, T. S., Alexander, B. and Lin, J.-T.: Global distribution of sea salt aerosols: new constraints from in situ and remote sensing observations, , doi:10.5194/acp-11-3137-2011, 2011.

Jimenez, J. L., Canagaratna, M. R., Donahue, N. M., Prevot, A. S. H., Zhang, Q., Kroll, J. H., DeCarlo, P. F., Allan, J. D., Coe, H., Ng, N. L., Aiken, A. C., Docherty, K. S., Ulbrich, I. M., Grieshop, A. P., Robinson, A. L., Duplissy, J., Smith, J. D., Wilson, K. R., Lanz, V. A., Hueglin, C., Sun, Y. L., Tian, J., Laaksonen, A., Raatikainen, T., Rautiainen, J., Vaattovaara, P., Ehn, M., Kulmala, M., Tomlinson, J. M., Collins, D. R., Cubison, M. J., Dunlea, E. J., Huffman, J. A., Onasch, T. B., Alfarra, M. R., Williams, P. I., Bower, K., Kondo, Y., Schneider, J., Drewnick, F., Borrmann, S., Weimer, S., Demerjian, K., Salcedo, D., Cottrell, L., Griffin, R., Takami, A., Miyoshi, T., Hatakeyama, S., Shimono, A., Sun, J. Y., Zhang, Y. M., Dzepina, K., Kimmel, J. R., Sueper, D., Jayne, J. T., Herndon, S. C., Trimborn, A. M., Williams, L. R., Wood, E. C., Middlebrook, A. M., Kolb, C. E., Baltensperger, U. and Worsnop, D. R.: Evolution of organic aerosols in the atmosphere, Science, 326(5959), 1525–1529, 2009.

Kacenelenbogen, M., Vaughan, M. A., Redemann, J., Hoff, R. M., Rogers, R. R., Ferrare, R. A., Russell, P. B., Hostetler, C. A., Hair, J. W. and Holben, B. N.: An accuracy assessment of the CALIOP/CALIPSO version 2/version 3 daytime aerosol extinction product based on a detailed multi-sensor, multi-platform case study, Atmos. Chem. Phys., 11(8), 3981–4000, 2011.

Katich, J. M., Samset, B. H., Bui, T. P., Dollner, M., Froyd, K. D., Campuzano-Jost, P., Nault, B. A., Schroder, J. C., Weinzierl, B. and Schwarz, J. P.: Strong Contrast in Remote Black Carbon Aerosol Loadings Between the Atlantic and Pacific Basins, J. Geophys. Res. D: Atmos., 123(23), 13,386–13,395, 2018.

Klein, S. A. and Hartmann, D. L.: The Seasonal Cycle of Low Stratiform Clouds, J. Clim., 6, 1587–1606, 1993.

Koch, D., Schulz, M., Kinne, S., McNaughton, C., Spackman, J. R., Balkanski, Y., Bauer, S., Berntsen, T., Bond, T. C., Boucher, O., Chin, M., Clarke, A., Luca, N. D., Dentener, F., Diehl, T., Dubovik, O., Easter, R., Fahey, D. W., Feichter, J., Fillmore, D., Freitag, S., Ghan, S., Ginoux, P., Gong, S., Horowitz,

L., Iversen, T., Kirkevåg, A., Klimont, Z., Kondo, Y., Krol, M., Liu, X., Miller, R., Montanaro, V., Moteki, N., Myhre, G., Penner, J. E., Perlwitz, J., Pitari, G., Reddy, S., Sahu, L., Sakamoto, H., Schuster, G., Schwarz, J. P., Seland, Ø., Stier, P., Takegawa, N., Takemura, T., Textor, C., van Aardenne, J. A. and Zhao, Y.: Evaluation of black carbon estimations in global aerosol models, Atmos. Chem. Phys., 9(22), 9001–9026, 2009.

Koepke, P., Hess, M., Schult, I. and Shettle, E.: Global Aerosol Data Set, Rep. 243, Max Planck Institute for Meteorology, 1997.

Larson, V. E.: CLUBB-SILHS: A parameterization of subgrid variability in the atmosphere, arXiv [physics.ao-ph] [online] Available from: http://arxiv.org/abs/1711.03675, 2017.

Larson, V. E. and Golaz, J.-C.: Using Probability Density Functions to Derive Consistent Closure Relationships among Higher-Order Moments, Monthly Weather Review, 133(4), 1023–1042, doi:10.1175/mwr2902.1, 2005.

LeBlanc, S. E., Redemann, J., Flynn, C., Pistone, K., Kacenelenbogen, M., Segal-Rosenheimer, M., Shinozuka, Y., Dunagan, S., Dahlgren, R. P., Meyer, K., Podolske, J., Howell, S. G., Freitag, S., Small-Griswold, J., Holben, B., Diamond, M., Formenti, P., Piketh, S., Maggs-Kölling, G., Gerber, M. and Namwoonde, A.: Above Cloud Aerosol Optical Depth from airborne observations in the South-East Atlantic, , doi:10.5194/acp-2019-43, 2019.

Lim, K.-S. S., Fan, J., Leung, L. R., Ma, P.-L., Singh, B., Zhao, C., Zhang, Y., Zhang, G. and Song, X.: Investigation of aerosol indirect effects using a cumulus microphysics parameterization in a regional climate model: INVESTIGATION OF AIE ON REGIONAL CLIMATE, J. Geophys. Res. D: Atmos., 119(2), 906–926, 2014.

Liu, H., Jacob, D. J., Bey, I. and Yantosca, R. M.: Constraints from210Pb and7Be on wet deposition and transport in a global three-dimensional chemical tracer model driven by assimilated meteorological fields, Journal of Geophysical Research: Atmospheres, 106(D11), 12109–12128, doi:10.1029/2000jd900839, 2001.

Liu, X., Easter, R. C., Ghan, S. J., Zaveri, R., Rasch, P., Shi, X., -F. Lamarque, J., Gettelman, A., Morrison, H., Vitt, F., Conley, A., Park, S., Neale, R., Hannay, C., Ekman, A. M. L., Hess, P., Mahowald, N., Collins, W., Iacono, M. J., Bretherton, C. S., Flanner, M. G. and Mitchell, D.: Toward a Minimal Representation of Aerosols in Climate Models: Description and Evaluation in the Community Atmosphere Model CAM5, Geoscientific Model Development, 5(3), 709, 2012.

Liu, X., Ma, P.-L., Wang, H., Tilmes, S., Singh, B., Easter, R. C., Ghan, S. J. and Rasch, P. J.: Description and evaluation of a new four-mode version of the Modal Aerosol Module (MAM4) within version 5.3 of the Community Atmosphere Model, Geoscientific Model Development (Online), 9(PNNL-SA-110649) [online] Available from: https://www.osti.gov/biblio/1243191, 2016.

Liu, X., Huey, L. G., Yokelson, R. J., Selimovic, V., Simpson, I. J., Müller, M., Jimenez, J. L., Campuzano-Jost, P., Beyersdorf, A. J., Blake, D. R., Butterfield, Z., Choi, Y., Crounse, J. D., Day, D. A.,

Diskin, G. S., Dubey, M. K., Fortner, E., Hanisco, T. F., Hu, W., King, L. E., Kleinman, L., Meinardi, S., Mikoviny, T., Onasch, T. B., Palm, B. B., Peischl, J., Pollack, I. B., Ryerson, T. B., Sachse, G. W., Sedlacek, A. J., Shilling, J. E., Springston, S., St. Clair, J. M., Tanner, D. J., Teng, A. P., Wennberg, P. O., Wisthaler, A. and Wolfe, G. M.: Airborne measurements of western U.S. wildfire emissions: Comparison with prescribed burning and air quality implications, J. Geophys. Res. D: Atmos., 122(11), 6108–6129, 2017.

Liu, Z., Winker, D., Omar, A., Vaughan, M., Kar, J., Trepte, C., Hu, Y. and Schuster, G.: Evaluation of CALIOP 532 nm aerosol optical depth over opaque water clouds, Atmos. Chem. Phys., 15(3), 1265–1288, 2015.

Lock, A. P., Brown, A. R., Bush, M. R., Martin, G. M. and Smith, R. N. B.: A New Boundary Layer Mixing Scheme. Part I: Scheme Description and Single-Column Model Tests, Mon. Weather Rev., 128(9), 3187–3199, 2000.

Lucchesi, R.: File Specification for GEOS-5 FP-IT (Forward Processing for Instrument Teams), [online] Available from: https://ntrs.nasa.gov/search.jsp?R=20150001438 (Accessed 11 April 2019), 2013.

Lu, Z., Liu, X., Zhang, Z., Zhao, C., Meyer, K., Rajapakshe, C., Wu, C., Yang, Z. and Penner, J. E.: Biomass smoke from southern Africa can significantly enhance the brightness of stratocumulus over the southeastern Atlantic Ocean, Proc. Natl. Acad. Sci. U. S. A., 115(12), 2924–2929, 2018.

Mallet, M., Nabat, P., Zuidema, P., Redemann, J., Sayer, A. M., Stengel, M., Schmidt, S., Cochrane, S., Burton, S., Ferrare, R., Meyer, K., Saide, P., Jethva, H., Torres, O., Wood, R., Saint Martin, D., Roehrig, R., Hsu, C. and Formenti, P.: Simulation of the transport, vertical distribution, optical properties and radiative impact of smoke aerosols with the ALADIN regional climate model during the ORACLES-2016 and LASIC experiments, Atmos. Chem. Phys., 19(7), 4963–4990, 2019.

Ma, P.-L., Rasch, P. J., Fast, J. D., Easter, R. C., Gustafson, W. I., Jr., Liu, X., Ghan, S. J. and Singh, B.: Assessing the CAM5 physics suite in the WRF-Chem model: implementation, resolution sensitivity, and a first evaluation for a regional case study, Geoscientific Model Development, 7(3), 755–778, 2014.

McNaughton, C. S., Clarke, A. D., Freitag, S., Kapustin, V. N., Kondo, Y., Moteki, N., Sahu, L., Takegawa, N., Schwarz, J. P., Spackman, J. R., Watts, L., Diskin, G., Podolske, J., Holloway, J. S., Wisthaler, A., Mikoviny, T., de Gouw, J., Warneke, C., Jimenez, J., Cubison, M., Howell, S. G., Middlebrook, A., Bahreini, R., Anderson, B. E., Winstead, E., Thornhill, K. L., Lack, D., Cozic, J. and Brock, C. A.: Absorbing aerosol in the troposphere of the Western Arctic during the 2008 ARCTAS/ARCPAC airborne field campaigns, Atmos. Chem. Phys., 11(15), 7561–7582, 2011.

Molod, A., Takacs, L., Suarez, M. and Bacmeister, J.: Development of the GEOS-5 atmospheric general circulation model: evolution from MERRA to MERRA2, Geoscientific Model Development, 8(5), 1339–1356, 2015.

Morcrette, J.-J.: Description of the radiation scheme in the ECMWF model, , doi:10.21957/I1KILJZZE, 1989.

1 Morrison, H. and Gettelman, A.: A New Two-Moment Bulk Stratiform Cloud Microphysics Scheme in
2 the Community Atmosphere Model, Version 3 (CAM3). Part I: Description and Numerical Tests, J.
3 Clim., 21(15), 3642–3659, 2008.

4 Myhre, G., Berntsen, T. K., Haywood, J. M., Sundet, J. K., Holben, B. N., Johnsrud, M. and Stordal, F.:
5 Modeling the solar radiative impact of aerosols from biomass burning during the Southern African
6 Regional Science Initiative (SAFARI-2000) experiment, J. Geophys. Res. D: Atmos., 108(D13) [online]
7 Available from: https://onlinelibrary.wiley.com/doi/pdf/10.1029/2002JD002313, 2003.

8 Myhre, G., Samset, B. H., Schulz, M., Balkanski, Y., Bauer, S., Berntsen, T. K., Bian, H., Bellouin, N.,
9 Chin, M., Diehl, T., Easter, R. C., Feichter, J., Ghan, S. J., Hauglustaine, D., Iversen, T., Kinne, S.,
10 Kirkevåg, A., Lamarque, J.-F., Lin, G., Liu, X., Lund, M. T., Luo, G., Ma, X., van Noije, T., Penner, J.
11 E., Rasch, P. J., Ruiz, A., Seland, Ø., Skeie, R. B., Stier, P., Takemura, T., Tsigaridis, K., Wang, P.,
12 Wang, Z., Xu, L., Yu, H., Yu, F., Yoon, J.-H., Zhang, K., Zhang, H. and Zhou, C.: Radiative forcing of
13 the direct aerosol effect from AeroCom Phase II simulations, Atmos. Chem. Phys., 13(4), 1853–1877,
14 2013.

15 NASA Ames Earth Science Project Office: ORACLES Science Team: Suite of Aerosol, Cloud, and
16 Related Data Acquired Aboard ER2 During ORACLES 2016, Version 1, ,
17 doi:10.5067/Suborbital/ORACLES/ER2/2016_V1, 2017a.

18 NASA Ames Earth Science Project Office: ORACLES Science Team: Suite of Aerosol, Cloud, and
19 Related Data Acquired Aboard P3 During ORACLES 2016, Version 1, ,
20 doi:10.5067/Suborbital/ORACLES/P3/2016_V1, 2017b.

21 Neale, R. B., Chen, C.-C., Gettelman, A., Lauritzen, P. H., Park, S., Williamson, D. L., Conley, A. J.,
22 Garcia, R., Kinnison, D., Lamarque, J.-F. and Others: Description of the NCAR community atmosphere
23 model (CAM 5.0), NCAR Tech. Note NCAR/TN-486+ STR, 1(1), 1–12, 2010.

24 Park, R. J.: Sources of carbonaceous aerosols over the United States and implications for natural
25 visibility, J. Geophys. Res., 108(D12), 23,073, 2003.

26 Pauly, R. M., Yorks, J. E., Hlavka, D. L., McGill, M. J., Amiridis, V., Palm, S. P., Rodier, S. D.,
27 Vaughan, M. A., Selmer, P. A., Kupchock, A. W., Baars, H. and Gialitaki, A.: Cloud Aerosol Transport
28 System (CATS) 1064 nm Calibration and Validation, , doi:10.5194/amt-2019-172, 2019.

29 Peers, F., Waquet, F., Cornet, C., Dubuisson, P., Ducos, F., Goloub, P., Szczap, F., Tanré, D. and
30 Thieuleux, F.: Absorption of aerosols above clouds from POLDER/PARASOL measurements and
31 estimation of their direct radiative effect, Atmos. Chem. Phys., 15(8), 4179–4196, 2015.

32 Petrenko, M., Kahn, R., Chin, M. and Limbacher, J.: Refined Use of Satellite Aerosol Optical Depth
33 Snapshots to Constrain Biomass Burning Emissions in the GOCART Model: Refined BB Emission
34 Correction for GOCART, J. Geophys. Res. D: Atmos., 122(20), 10,983–11,004, 2017.

35 Petters, M. D. and Kreidenweis, S. M.: A single parameter representation of hygroscopic growth and

cloud condensation nucleus activity, Atmos. Chem. Phys., 7(8), 1961–1971, 2007.

Pistone, K., Redemann, J., Doherty, S., Zuidema, P., Burton, S., Cairns, B., Cochrane, S., Ferrare, R., Flynn, C., Freitag, S., Howell, S., Kacenelenbogen, M., LeBlanc, S., Liu, X., Schmidt, K. S., Sedlacek, A. J., III, Segal-Rosenhaimer, M., Shinozuka, Y., Stamnes, S., van Diedenhoven, B., Van Harten, G. and Xu, F.: Intercomparison of biomass burning aerosol optical properties from in-situ and remote-sensing instruments in ORACLES-2016, Atmos. Chem. Phys. Discuss., 1–46, 2019.

Provencal, R., Gupta, M., Owano, T. G., Baer, D. S., Ricci, K. N., O'Keefe, A. and Podolske, J. R.: Cavity-enhanced quantum-cascade laser-based instrument for carbon monoxide measurements, Appl. Opt., 44(31), 6712, 2005.

Rajapakshe, C., Zhang, Z., Yorks, J. E., Yu, H., Tan, Q., Meyer, K., Platnick, S. and Winker, D. M.: Seasonally transported aerosol layers over southeast Atlantic are closer to underlying clouds than previously reported: Smoke to Cloud Distance in SE Atlantic, Geophys. Res. Lett., 44(11), 5818–5825, 2017.

Randles, C. A., da Silva, A. M., Buchard, V., Colarco, P. R., Darmenov, A., Govindaraju, R., Smirnov, A., Holben, B., Ferrare, R., Hair, J., Shinozuka, Y. and Flynn, C. J.: The MERRA-2 Aerosol Reanalysis, 1980 Onward. Part I: System Description and Data Assimilation Evaluation, J. Clim., 30(17), 6823–6850, 2017.

Rasch, P. J., Xie, S., Ma, P. -L, Lin, W., Wang, H., Tang, Q., Burrows, S. M., Caldwell, P., Zhang, K., Easter, R. C., Cameron-Smith, P., Singh, B., Wan, H., Golaz, J. -C, Harrop, B. E., Roesler, E., Bacmeister, J., Larson, V. E., Evans, K. J., Qian, Y., Taylor, M., Leung, L. R., Zhang, Y., Brent, L., Branstetter, M., Hannay, C., Mahajan, S., Mametjanov, A., Neale, R., Richter, J. H., Yoon, J. -H, Zender, C. S., Bader, D., Flanner, M., Foucar, J. G., Jacob, R., Keen, N., Klein, S. A., Liu, X., Salinger, A. G., Shrivastava, M. and Yang, Y.: An Overview of the Atmospheric Component of the Energy Exascale Earth System Model, J. Adv. Model. Earth Syst., doi:10.1029/2019MS001629, 2019.

Reddington, C. L., Carslaw, K. S., Stier, P., Schutgens, N., Coe, H., Liu, D., Allan, J., Browse, J., Pringle, K. J., Lee, L. A., Yoshioka, M., Johnson, J. S., Regayre, L. A., Spracklen, D. V., Mann, G. W., Clarke, A., Hermann, M., Henning, S., Wex, H., Kristensen, T. B., Leaitch, W. R., Pöschl, U., Rose, D., Andreae, M. O., Schmale, J., Kondo, Y., Oshima, N., Schwarz, J. P., Nenes, A., Anderson, B., Roberts, G. C., Snider, J. R., Leck, C., Quinn, P. K., Chi, X., Ding, A., Jimenez, J. L. and Zhang, Q.: The Global Aerosol Synthesis and Science Project (GASSP): Measurements and Modeling to Reduce Uncertainty, Bull. Am. Meteorol. Soc., 98(9), 1857–1877, 2017.

Redemann, Wood, Zuidema, Doherty, Luna, LeBlanc, Diamond, Shinozuka, Ueyama, Pfister, DaSilva, Longo, Kacenelenbogen, Knox, Piketh, Haywood, Formenti, Mallet, Stier, Ackerman, Carmichael, Saide, Howell, Cairns, Knobelspiesse, Tanelli, L'Ecuyer, McFarquhar, Poellot, Nenes, Kacarab, Pui Shan Wong, Small-Griswold, Thornhill, Noone, Podolske, Schmidt, Sedlacek, Lang, Stith, Segal-Rozenhaimer, Hostetler, Ferrare, Burton, Diner, Platnick, Myers, Meyer, Spangenberg, Ian Chang: An overview of the ORACLES (ObseRvations of Aerosols above CLouds and their intEractionS) project: aerosol-cloud-radiation interactions in the Southeast Atlantic basin, in preparation.

Regayre, L. A., Johnson, J. S., Yoshioka, M., Pringle, K. J., Sexton, D. M. H., Booth, B. B. B., Lee, L. A., Bellouin, N. and Carslaw, K. S.: Aerosol and physical atmosphere model parameters are both important sources of uncertainty in aerosol ERF, Atmos. Chem. Phys., 18(13), 9975–10006, 2018.

Rienecker, M. M., Suarez, M. J., Todling, R., Bacmeister, J., Takacs, L., -C. Liu, H., Gu, W., Sienkiewicz, M., Koster, R. D., Gelaro, R., Stajner, I. and Nielsen, J. E.: The GEOS-5 Data Assimilation System— Documentation of Versions 5.0.1, 5.1.0, and 5.2.0, [online] Available from: https://gmao.gsfc.nasa.gov/pubs/docs/Rienecker369.pdf, 2008.

Rogers, R. R., Hair, J. W., Hostetler, C. A., Ferrare, R. A., Obland, M. D., Cook, A. L., Harper, D. B., Burton, S. P., Shinozuka, Y., McNaughton, C. S., Clarke, A. D., Redemann, J., Russell, P. B., Livingston, J. M. and Kleinman, L. I.: NASA LaRC airborne high spectral resolution lidar aerosol measurements during MILAGRO: observations and validation, Atmos. Chem. Phys., 9(14), 4811–4826, 2009.

Saide, P. E., Thompson, G., Eidhammer, T., da Silva, A. M., Bradley Pierce, R. and Carmichael, G. R.: Assessment of biomass burning smoke influence on environmental conditions for multiyear tornado outbreaks by combining aerosol-aware microphysics and fire emission constraints, Journal of Geophysical Research: Atmospheres, 121(17), 10,294–10,311, doi:10.1002/2016jd025056, 2016.

Sakaeda, N., Wood, R. and Rasch, P. J.: Direct and semidirect aerosol effects of southern African biomass burning aerosol, J. Geophys. Res., 116(D12), doi:10.1029/2010jd015540, 2011.

Schwarz, J. P., Gao, R. S., Fahey, D. W., Thomson, D. S., Watts, L. A., Wilson, J. C., Reeves, J. M., Darbeheshti, M., Baumgardner, D. G., Kok, G. L., Chung, S. H., Schulz, M., Hendricks, J., Lauer, A., Kärcher, B., Slowik, J. G., Rosenlof, K. H., Thompson, T. L., Langford, A. O., Loewenstein, M. and Aikin, K. C.: Single-particle measurements of midlatitude black carbon and light-scattering aerosols from the boundary layer to the lower stratosphere, J. Geophys. Res., 111(D16), D16207, doi:10.1029/2006JD007076, 2006.

Schwarz, J. P., Spackman, J. R., Gao, R. S., Perring, A. E., Cross, E., Onasch, T. B., Ahern, A., Wrobel, W., Davidovits, P., Olfert, J., Dubey, M. K., Mazzoleni, C. and Fahey, D. W.: The Detection Efficiency of the Single Particle Soot Photometer, Aerosol Sci. Technol., 44(8), 612–628, 2010.

Shank, L. M., Howell, S., Clarke, A. D., Freitag, S., Brekhovskikh, V., Kapustin, V., McNaughton, C., Campos, T. and Wood, R.: Organic matter and non-refractory aerosol over the remote Southeast Pacific: oceanic and combustion sources, Atmos. Chem. Phys., 12(1), 557–576, 2012.

Shipley, S. T., Tracy, D. H., Eloranta, E. W., Trauger, J. T., Sroga, J. T., Roesler, F. L. and Weinman, J. A.: High spectral resolution lidar to measure optical scattering properties of atmospheric aerosols. 1: Theory and instrumentation, Appl. Opt., AO, 22(23), 3716–3724, 1983.

Song, X. and Zhang, G. J.: Microphysics parameterization for convective clouds in a global climate model: Description and single-column model tests, J. Geophys. Res., 116(D2), 6837, 2011.

Stephens, M., Turner, N. and Sandberg, J.: Particle Identification by Laser-Induced Incandescence in a

1   Solid-State Laser Cavity, Appl. Opt., 42(19), 3726–3736, 2003.

2   Stier, P., Schutgens, N. A. J., Bellouin, N., Bian, H., Boucher, O., Chin, M., Ghan, S., Huneeus, N.,
3   Kinne, S., Lin, G., Ma, X., Myhre, G., Penner, J. E., Randles, C. A., Samset, B., Schulz, M., Takemura,
4   T., Yu, F., Yu, H. and Zhou, C.: Host model uncertainties in aerosol radiative forcing estimates: results
5   from the AeroCom Prescribed intercomparison study, Atmos. Chem. Phys., 13(6), 3245–3270, 2013.

6   Sueper, D.: ToF-AMS Software Downloads, online available at:
7   http://cires.colorado.edu/jimenezgroup/ToFAMSResources/ToFSoftware/ index.html, accessed February
8   2018, 2018.

9   Swap, R. J., Annegarn, H. J., Suttles, J. T., King, M. D., Platnick, S., Privette, J. L. and Scholes, R. J.:
10   Africa burning: A thematic analysis of the Southern African Regional Science Initiative (SAFARI 2000),
11   J. Geophys. Res. D: Atmos., 108(D13), doi:10.1029/2003jd003747, 2003.

12   Textor, C., Schulz, M., Guibert, S., Kinne, S., Balkanski, Y., Bauer, S., Berntsen, T., Berglen, T.,
13   Boucher, O., Chin, M. and Others: Analysis and quantification of the diversities of aerosol life cycles
14   within AeroCom, Atmos. Chem. Phys., 6(7), 1777–1813, 2006.

15   Virkkula, A.: Correction of the Calibration of the 3-wavelength Particle Soot Absorption Photometer (3λ
16   PSAP), Aerosol Sci. Technol., 44(8), 706–712, 2010.

17   Voldoire, A., Decharme, B., Pianezze, J., Lebeaupin Brossier, C., Sevault, F., Seyfried, L., Garnier, V.,
18   Bielli, S., Valcke, S., Alias, A., Accensi, M., Ardhuin, F., Bouin, M.-N., Ducrocq, V., Faroux, S.,
19   Giordani, H., Léger, F., Marsaleix, P., Rainaud, R., Redelsperger, J.-L., Richard, E. and Riette, S.:
20   SURFEX v8.0 interface with OASIS3-MCT to couple atmosphere with hydrology, ocean, waves and sea-
21   ice models, from coastal to global scales, Geoscientific Model Development, 10(11), 4207–4227, 2017.

22   Wang, J.: Geostationary satellite retrievals of aerosol optical thickness during ACE-Asia, J. Geophys.
23   Res., 108(D23), 17,969, 2003a.

24   Wang, J.: GOES 8 retrieval of dust aerosol optical thickness over the Atlantic Ocean during PRIDE, J.
25   Geophys. Res., 108(D19), 57, 2003b.

26   Wang, Q., Jacob, D. J., Fisher, J. A., Mao, J., Leibensperger, E. M., Carouge, C. C., Sager, P. L., Kondo,
27   Y., Jimenez, J. L., Cubison, M. J. and Doherty, S. J.: Sources of carbonaceous aerosols and deposited
28   black carbon in the Arctic in winter-spring: implications for radiative forcing, Atmos. Chem. Phys.,
29   11(23), 12453–12473, 2011.

30   Wang, Q., Jacob, D. J., Spackman, J. R., Perring, A. E., Schwarz, J. P., Moteki, N., Marais, E. A., Ge, C.,
31   Wang, J. and Barrett, S. R. H.: Global budget and radiative forcing of black carbon aerosol: Constraints
32   from pole-to-pole (HIPPO) observations across the Pacific, J. Geophys. Res. D: Atmos., 119(1), 195–206,
33   2014.

34   Waquet, F., Peers, F., Ducos, F., Goloub, P., Platnick, S., Riedi, J., Tanré, D. and Thieuleux, F.: Global

analysis of aerosol properties above clouds, Geophys. Res. Lett., 40(21), 5809–5814, 2013.

Wesely, M. L.: Parameterization of surface resistances to gaseous dry deposition in regional-scale numerical models, Atmospheric Environment (1967), 23(6), 1293–1304, doi:10.1016/0004-6981(89)90153-4, 1989.

Wilson, D. R. and Ballard, S. P.: A microphysically based precipitation scheme for the UK meteorological office unified model, Q.J Royal Met. Soc., 125(557), 1607–1636, 1999.

Wilson, D. R., Bushell, A. C., Kerr-Munslow, A. M., Price, J. D. and Morcrette, C. J.: PC2: A prognostic cloud fraction and condensation scheme. I: Scheme description, Q.J.R. Meteorol. Soc., 134(637), 2093–2107, 2008.

Wood, R., Mechoso, C. R., Bretherton, C. S., Weller, R. A., Huebert, B., Straneo, F., Albrecht, B. A., Coe, H., Allen, G., Vaughan, G. and Others: The VAMOS ocean-cloud-atmosphere-land study regional experiment (VOCALS-REx): goals, platforms, and field operations, Atmos. Chem. Phys., 11(2), 627–654, 2011.

Wyant, M. C., Wood, R., Bretherton, C. S., Mechoso, C. R., Bacmeister, J., Balmaseda, M. A., Barrett, B., Codron, F., Earnshaw, P., Fast, J., Hannay, C., Kaiser, J. W., Kitagawa, H., Klein, S. A., Köhler, M., Manganello, J., Pan, H.-L., Sun, F., Wang, S. and Wang, Y.: The PreVOCA experiment: modeling the lower troposphere in the Southeast Pacific, Atmos. Chem. Phys., 10(10), 4757–4774, 2010.

Wyant, M. C., Bretherton, C. S., Wood, R., Carmichael, G. R., Clarke, A., Fast, J., George, R., Gustafson, W. I., Jr., Hannay, C., Lauer, A., Lin, Y., Morcrette, J.-J., Mulcahy, J., Saide, P. E., Spak, S. N. and Yang, Q.: Global and regional modeling of clouds and aerosols in the marine boundary layer during VOCALS: the VOCA intercomparison, Atmos. Chem. Phys., 15(1), 153–172, 2015.

Xie, S., Lin, W., Rasch, P. J., Ma, P.-L., Neale, R., Larson, V. E., Qian, Y., Bogenschutz, P. A., Caldwell, P., Cameron-Smith, P., Golaz, J.-C., Mahajan, S., Singh, B., Tang, Q., Wang, H., Yoon, J.-H., Zhang, K. and Zhang, Y.: Understanding Cloud and Convective Characteristics in Version 1 of the E3SM Atmosphere Model, Journal of Advances in Modeling Earth Systems, 10(10), 2618–2644, doi:10.1029/2018ms001350, 2018.

Zaveri, R. A. and Peters, L. K.: A new lumped structure photochemical mechanism for large-scale applications, J. Geophys. Res., 104(D23), 30387–30415, 1999.

Zhang, G. J. and McFarlane, N. A.: Sensitivity of climate simulations to the parameterization of cumulus convection in the Canadian climate centre general circulation model, Atmosphere-Ocean, 33(3), 407–446, 1995.

Zhang, L., Gong, S., Padro, J. and Barrie, L.: A size-segregated particle dry deposition scheme for an atmospheric aerosol module, Atmos. Environ., 35(3), 549–560, 2001.

Zhang, Y., Zhang, X., Wang, K., He, J., Leung, L. R., Fan, J. and Nenes, A.: Incorporating an advanced

aerosol activation parameterization into WRF-CAM5: Model evaluation and parameterization intercomparison: An Advanced Aerosol Activation Scheme, J. Geophys. Res. D: Atmos., 120(14), 6952–6979, 2015.

Zhu, C., Kobayashi, H., Kanaya, Y. and Saito, M.: Size-dependent validation of MODIS MCD64A1 burned area over six vegetation types in boreal Eurasia: Large underestimation in croplands, Sci. Rep., 7(1), 4181, 2017.

Zuidema, P., Redemann, J., Haywood, J., Wood, R., Piketh, S., Hipondoka, M. and Formenti, P.: Smoke and clouds above the southeast Atlantic: Upcoming field campaigns probe absorbing aerosol's impact on climate, Bull. Am. Meteorol. Soc., 97(7), 1131–1135, 2016.

1   **Table 1. Specifications of the observations used in this study.**

Instrument [platform]	Primary measurement	Temporal resolution
SP2 [P3]	Black carbon mass per particle, 90–500 nm	Particle by particle
Time of Flight (ToF) – Aerodyne aerosol mass spectrometer (AMS) [P3]	Non−refractory aerosol composition (~ 50 to 500 nm vacuum aerodynamic diameter)	5s
UHSAS, ultra-high sensitivity aerosol spectrometer [P3]	Number size distribution for dry particle diameters between 60 and 1000 nm	1s
Nephelometer [P3]	Submicron dry particle scattering coefficient at 450, 550, 700 nm	6s
PSAP, particle soot absorption photometer [P3]	Submicron dry particle light absorption at 470, 530 and 660 nm	1-60s depending on concentration
4STAR, an airborne sun-/sky-photometer [P3]	Hyperspectral direct solar beam transmittance, AOD; values at 550 nm	1s
HSRL-2, the NASA Langley 2nd generation airborne High Spectral Resolution Lidar [ER2]	Aerosol backscattering and extinction coefficients, values at 532 nm	10s for aerosol backscatter coefficient and 60s for aerosol extinction coefficient
CO/CO2/H2O Analyzer [P3]	Carbon monoxide	1s

1   **Table 2. Model specifications.**

Model	Domain extent	Horizontal grid spacing	Vertical levels (> and < 700 hPa)	initializing meteorology	Initialization frequency	Aerosol scheme	PMBL scheme	Fire emissions source	Emission temporal resolution
WRF-CAM5	41S-14N, 34W-51E	36 km	75, 50	NCEP Final Analysis	5 days	MAM3	Bretherton and Park (2009)	QFED2	Daily
GEOS-5	Global	25 by 31 km	72, 17	MERRA-2	Daily	AeroChem (GOCART)	TURBDAY	QFED2	Daily
GEOS-Chem	Global	2.5° by 2 (lon, lat)	17, 55	GEOS-FP	Hourly	GEOS-Chem standard	VDIFF: non-local scheme formulated by Holtslag and Boville (1993)	QFED2	Daily
EAM-E3SM	Global	100 km	72, 17	ERA-INT	Every 3 hours	MAM4	CLUBB (Larson and Golaz, 2005)	GFED*	Monthly
Unified Model	Global	61 by 92 km	65, 20	ERA-INT	Every 6 hours	GLOMAP-mode	Lock et al. (2000)	FEER	Daily
ALADIN-Climate	37S-9N; 33W-45E	12 km	34, 6	ERA-INT	Once	Interactive		GFED	Monthly

2   *IPCC AR5 emissions, based on GFED emissions averaged between 1997-2002.

1 **Table 3. Comparison of flight-day values to the monthly-mean climatology formulated from**
2 **the same model. Shown are the mean bias (MB), and root-mean-square deviation (RMSD),**
3 **as well as their ratio (%) to the monthly mean.**

	WRF-CAM5		GEOS-5	
	MB	RMSD	MB	RMSD
Smoke Top Height (m) simulated as observed by HSRL-2 on ER2				
	+125	500	+369	505
	(+3%)	(11%)	(+11%)	(15%)
Smoke Base Height (m) simulated as observed by HSRL-2 on ER2				
	+371	426	+103	292
	(+29%)	(33%)	(+8%)	(23%)
Black Carbon Mass (ng m^{-3})				
3-6 km	-4.5	182.5	-1.8	198.2
	(-1%)	(27%)	(-0%)	(30%)
FT≤ 3km	+161.1	319.3	-98.8	423.6
	(+25%)	(50%)	(-9%)	(38%)
MBL	+40.1	80.3	+82.1	354.2
	(+31%)	(63%)	(+21%)	(93%)
Organic Aerosol Mass (ug m^{-3})				
3-6 km	-0.0	1.5	+0.0	2.9
	(-0%)	(27%)	(+0%)	(32%)
FT≤ 3km	+1.3	2.6	-1.6	6.2
	(+25%)	(50%)	(-10%)	(40%)

MBL	+0.3 (+36%)	0.6 (70%)	+1.0 (+19%)	4.9 (92%)

Sulfate Aerosol Mass (ug m^{-3})

3-6 km	-0.1 (-4%)	0.2 (19%)	--	--
FT≤ 3km	+0.2 (+17%)	0.4 (31%)	--	--
MBL	+0.1 (+13%)	0.3 (44%)	--	--

Volumetric Mean Diameter (nm)

3-6 km	-7 (-3%)	10 (4%)	--	--
FT≤ 3km	-6 (-2%)	17 (6%)	--	--
MBL	-22 (-7%)	37 (12%)	--	--

Aerosol Optical Depth simulated as observed by HSRL-2 on ER2

Above clouds	+0.018 (+7%)	0.055 (21%)	+0.001 (+1%)	0.036 (16%)

Aerosol Optical Depth simulated as observed by 4STAR on P3

Above clouds	+0.031 (+12%)	0.048 (18%)	-0.019 (-9%)	0.057 (26%)

Extinction Coefficient (Mm^{-1}) simulated as observed by HSRL-2 on ER2

3-6 km	+3	12	+2	12
	(+7%)	(23%)	(+5%)	(30%)

Extinction Coefficient (Mm⁻¹) simulated as observed by neph+PSAP on P3

3-6 km	-1	13	-1	14
	(-3%)	(25%)	(-3%)	(33%)
FT≤ 3km	+11	22	-8	24
	(+22%)	(42%)	(-13%)	(39%)
MBL	-2	10	+7	67
	(-6%)	(32%)	(+6%)	(62%)

Scattering Ångström Exponent

3-6 km	+0.1	0.1	+0.0	0.0
	(+5%)	(6%)	(+0%)	(2%)
FT≤3km	+0.0	0.1	+0.0	0.1
	(+4%)	(12%)	(+2%)	(6%)
MBL	+0.1	0.2	+0.1	0.2
	(+29%)	(44%)	(+10%)	(30%)

Absorption Ångström Exponent

3-6 km	+0.0	0.0	+0.0	0.0
	(+1%)	(1%)	(+0%)	(0%)
FT≤3km	+0.0	0.0	-0.0	0.0
	(+0%)	(2%)	(-0%)	(1%)
MBL	+0.0	0.1	-0.0	0.0
	(+1%)	(5%)	(-0%)	(2%)

Single Scattering Albedo

3-6 km	-0.00	0.01	-0.00	0.01
	(-0%)	(1%)	(-0%)	(1%)

FT≤3k m	-0.01 (-1%)	0.01 (2%)	-0.00 (-0%)	0.01 (1%)
MBL	-0.02 (-2%)	0.03 (3%)	-0.01 (-1%)	0.01 (1%)

Carbon Monoxide (ppbv)

3-6 km	+0 (+0%)	23 (15%)	+0 (+0%)	22 (13%)
FT≤ 3km	+12 (+10%)	29 (23%)	-2 (-2%)	26 (16%)
MBL	+3 (+5%)	5 (7%)	+1 (+2%)	12 (15%)

2   The optical properties are at 500-550 nm. The values are for the P3 flights unless otherwise

3   noted, in the diagonally and horizontally aligned boxes.

1 **Table 4. The differences of box-average model values from the observations. Shown are the**
2 **mean bias (MB), and root-mean-square deviation (RMSD), as well as their ratio (%) to the**
3 **observed mean.**

	WRF-CAM5		GEOS-5		GEOS-Chem		EAM-E3SM		UM		ALADIN-Climate	
	MB	RMSD	MB	RMSD	MB	RMSD	MB	RMSD	MB	RMSD	MB	RMSD
Smoke Top Height (m) compared to HSRL-2 on ER2												
	-167	415	-456	596	-473	763	-114	460	+6	440	-176	830
	(-3%)	(9%)	(-9%)	(12%)	(-10%)	(16%)	(-2%)	(10%)	(+0%)	(9%)	(-4%)	(17%)
Smoke Base Height (m) compared to HSRL-2 on ER2												
	-422	553	-1401	1424	-877	938	-688	784	-616	709	-299	566
	(-21%)	(27%)	(-69%)	(70%)	(-43%)	(46%)	(-34%)	(38%)	(-31%)	(35%)	(-15%)	(28%)
Black Carbon Mass (ng m^{-3})												
3-6 km	+60.4	171.4	+47.4	206.1	+7.9	283.0	-256.6	287.1	-234.6	279.0	--	--
	(+10%)	(28%)	(+8%)	(34%)	(+1%)	(47%)	(-42%)	(47%)	(-39%)	(46%)		
FT ≤3km	-13.0	456.1	+162.1	527.5	-1.6	392.3	-524.8	655.9	-140.2	312.9	--	--
	(-2%)	(56%)	(+19%)	(62%)	(-0%)	(46%)	(-61%)	(77%)	(-16%)	(37%)		
MBL	-8.2	118.2	+288.3	552.8	+79.4	236.8	+2.7	97.7	-48.6	93.9	--	--
	(-5%)	(67%)	(+163%)	(313%)	(+45%)	(134%)	(+1%)	(52%)	(-28%)	(53%)		
Organic Aerosol Mass (ug m^{-3})												
3-6 km	+0.0	2.3	+3.5	5.0	+1.8	4.0	+5.3	5.7	-1.9	2.9	--	--
	(+0%)	(42%)	(+63%)	(89%)	(+32%)	(71%)	(+95%)	(103%)	(-34%)	(52%)		
FT ≤3km	+0.7	3.0	+7.7	9.2	+3.6	5.4	+2.8	4.1	+0.5	3.1	--	--
	(+12%)	(53%)	(+117%)	(140%)	(+55%)	(82%)	(+43%)	(62%)	(+8%)	(47%)		
MBL	+0.3	0.8	+5.4	8.9	+2.1	3.9	+3.7	5.1	+0.3	0.9	--	--
	(+26%)	(83%)	(+546%)	(901%)	(+210%)	(392%)	(+352%)	(494%)	(+27%)	(96%)		
Sulfate Aerosol Mass (ug m^{-3})												
3-6 km	+0.5	0.6	--	--	--	--	+0.2	0.3	-0.4	0.6	--	--
	(+67%)	(79%)					(+21%)	(43%)	(-56%)	(74%)		
FT ≤3km	+0.4	0.7	--	--	--	--	+0.1	0.5	-0.7	1.0	--	--
	(+37%)	(55%)					(+4%)	(42%)	(-56%)	(75%)		

	WRF-CAM5 MB	RMSD	GEOS-5 MB	RMSD	GEOS-Chem MB	RMSD	EAM-E3SM MB	RMSD	UM MB	RMSD	ALADIN-Climate MB	RMSD
MBL	-0.5 (-38%)	0.7 (60%)	--	--	--	--	+1.2 (+94%)	1.5 (121%)	-0.5 (-45%)	0.8 (67%)	--	--
Volumetric Mean Diameter (nm)												
3-6 km	+42 (+21%)	43 (21%)	--	--	--	--	--	--	+64/+121 (+32/+60%)	65/121 (32/60%)	--	--
FT ≤3km	+81 (+42%)	83 (43%)	--	--	--	--	--	--	+72/+116 (+37/+60%)	73/117 (37/60%)	--	--
MBL	+98 (+48%)	105 (52%)	--	--	--	--	--	--	+40/+215 (+20/+106%)	46/217 (23/107%)	--	--

	WRF-CAM5		GEOS-5		GEOS-Chem		EAM-E3SM		UM		ALADIN-Climate	
	MB	RMSD	MB	RMSD	MB	RMSD	MB	RMSD	MB	RMSD	MB	RMSD
Aerosol Optical Depth compared to HSRL-2 on ER2												
Above clouds	-0.042 (-12%)	0.077 (23%)	-0.101 (-30%)	0.123 (37%)	+0.138 (+42%)	0.189 (57%)	+0.069 (+21%)	0.093 (28%)	0.053 (-16%)	0.087 (26%)	-0.108 (-32%)	0.125 (37%)
Aerosol Optical Depth compared to 4STAR on P3												
Above clouds	-0.068 (-19%)	0.098 (28%)	-0.134 (-40%)	0.183 (55%)	+0.008 (+3%)	0.103 (31%)	+0.055 (+16%)	0.088 (26%)	-0.155 (-46%)	0.184 (55%)	-0.106 (-32%)	0.140 (42%)
Extinction Coefficient (Mm^{-1}) compared to HSRL-2 on ER2												
3-6 km	-16 (-23%)	23 (32%)	-28 (-38%)	32 (44%)	+24 (+33%)	33 (45%)	+1 (+1%)	17 (23%)	-43/-19 (-59/-26%)	49/23 (66/31%)	--	--
Extinction Coefficient (Mm^{-1}) compared to neph+PSAP on P3												
3-6 km	-25 (-34%)	29 (39%)	-34 (-46%)	36 (49%)	+5 (+6%)	41 (56%)	-8 (-11%)	20 (27%)	-57/-48 (-77/-65%)	58/49 (78/66%)	--	--
FT ≤3km	-8 (-11%)	34 (48%)	-22 (-29%)	39 (51%)	+14 (+18%)	33 (43%)	+6 (+8%)	21 (27%)	-40/-26 (-53/-35%)	49/35 (65/47%)	--	--

MBL	-13 (-32%)	23 (54%)	+73 (+175%)	119 (285%)	+54 (+128%)	75 (181%)	+104 (+269%)	115 (297%)	-18/+55 (-44/+132%)	27/64 (64/153%)	--	--
Scattering Ångström Exponent												
3-6 km	-0.6 (-35%)	0.6 (36%)	-0.1 (-4%)	0.1 (6%)	+0.0 (+0%)	0.1 (3%)	--	--	+0.0/-0.0 (+2/-2%)	0.1/0.1 (3/8%)	--	--
FT ≤3km	-0.8 (-45%)	0.8 (46%)	-0.0 (-1%)	0.1 (7%)	+0.1 (+3%)	0.1 (5%)	--	--	+0.0/-0.0 (+2/-1%)	0.1/0.1 (6/6%)	--	--
MBL	-0.7 (-53%)	0.8 (57%)	-0.7 (-52%)	0.8 (59%)	-0.5 (-34%)	0.7 (48%)	--	--	-0.4/-0.6 (-27/-40%)	0.6/0.7 (45/50%)	--	--
Absorption Ångström Exponent												
3-6 km	-0.4 (-27%)	0.4 (27%)	-0.4 (-27%)	0.4 (28%)	-0.4 (-25%)	0.4 (25%)	--	--	-0.1/-0.2 (-5/-10%)	0.1/0.2 (7/12%)	--	--
FT ≤3km	-0.5 (-30%)	0.5 (30%)	-0.4 (-27%)	0.4 (27%)	-0.4 (-23%)	0.4 (24%)	--	--	-0.1/-0.2 (-8/-10%)	0.1/0.2 (9/11%)	--	--
MBL	-0.3 (-23%)	0.6 (41%)	-0.2 (-16%)	0.6 (43%)	-0.3 (-22%)	0.7 (44%)	--	--	+0.0/-0.3 (+3/-20%)	0.5/0.8 (33/54%)	--	--
Single Scattering Albedo												
3-6 km	-0.03 (-3%)	0.03 (4%)	-0.01 (-2%)	0.02 (2%)	+0.07 (+8%)	0.07 (8%)	+0.02 (+3%)	0.03 (3%)	-0.07/-0.01 (-8/-2%)	0.07/0.02 (8/3%)	--	--
FT ≤3km	+0.01 (+1%)	0.02 (2%)	-0.00 (-0%)	0.01 (2%)	+0.08 (+10%)	0.08 (10%)	+0.08 (+9%)	0.08 (9%)	-0.03/+0.01 (-4/+1%)	0.04/0.02 (4/3%)	--	--
MBL	+0.03 (+4%)	0.07 (8%)	+0.08 (+9%)	0.10 (11%)	+0.10 (+11%)	0.11 (12%)	+0.08 (+8%)	0.09 (10%)	+0.07/+0.10 (+8/+12%)	0.09/0.11 (11/13%)	--	--

Carbon Monoxide (ppbv)

3-6 km	-37	44	-19	30	-38	45	--	--	--	--	--	--
	(-20%)	(23%)	(-10%)	(16%)	(-20%)	(24%)						
FT ≤3km	-25	44	-14	33	-9	36	--	--	--	--	--	--
	(-15%)	(27%)	(-8%)	(19%)	(-5%)	(21%)						
MBL	-20	24	-10	21	-4	19	--	--	--	--	--	--
	(-22%)	(26%)	(-11%)	(22%)	(-4%)	(20%)						

2 The optical properties are at 500-550 nm. The values are for the P3 flights unless otherwise

3 noted, in the diagonally and horizontally aligned boxes. The hyphens indicate products

4 unavailable. For UM the pair of values, where given, correspond to dry and ambient humidity

5 conditions in this order.
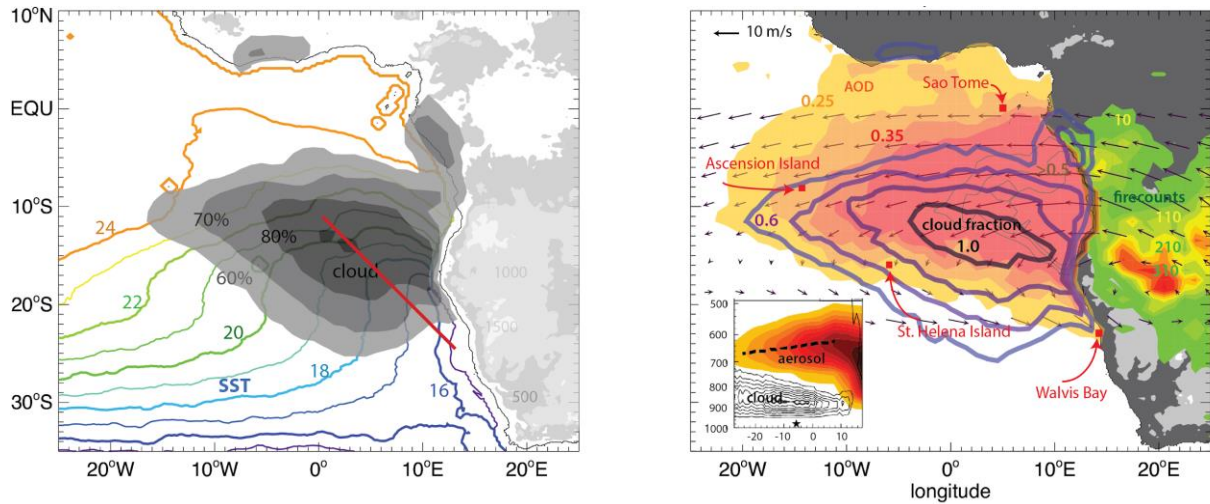
Fig. 1. (a) September 2003-2016 WindSat sea surface temperature climatology (colored contours) and 2000-2016 Terra MODIS low cloud fraction climatology (gray shaded contours), with the routine flight track superimposed (red line). (b) September-mean climatology of MODIS low-level cloud fraction (2002-2012; blue to black contours, 0.6-1.0 increments of 0.1), fine-mode aerosol optical depth (yellow-red shading indicates 0.25–0.45 in increments of 0.05 and very light black contour lines indicate 0.5–0.7 in increments of 0.1), and fire pixel counts (green–red shading, 50–310 fire counts per 1° box in increments of 50), and ERA-Interim 2002–2012 600-hPa winds (referenced at 10 m/s). Inset: September-mean a 6°S–17°S latitude cross-section of CALIOP smoke aerosol count (2006-2012) and CloudSat cloud fraction (2006-2010). The CloudSat cloud fraction are calculated following Stein et al. (2011). Right panel figure reproduced from Zuidema et al. (2016)**. © American Meteorological Society. Used with permission.**
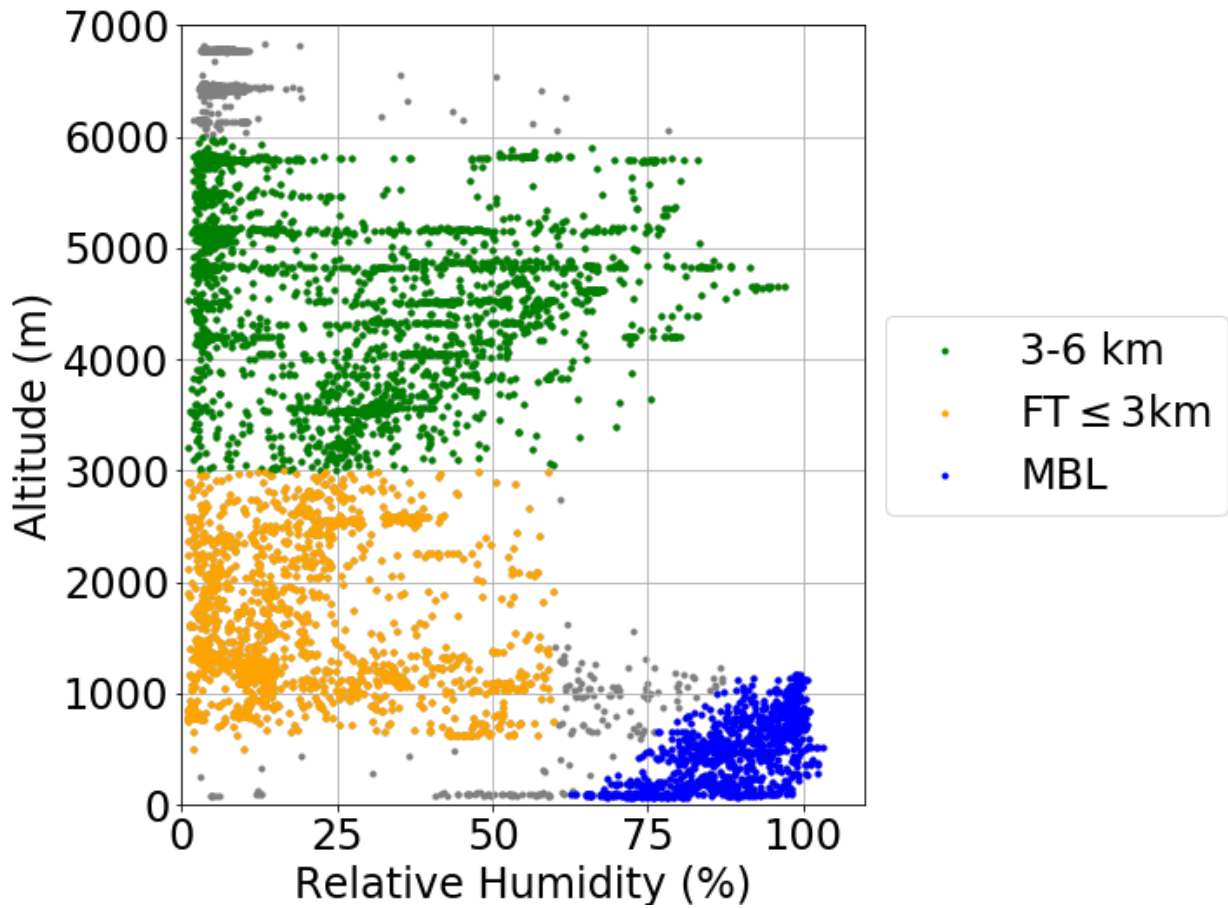
Fig. 2. Observed vertical profiles of relative humidity, derived from the dew point measurements. The blue, orange and green markers indicate MBL, the lower FT and mid FT, respectively, as defined in text. The grey markers indicate the data that do not belong to either group, most of them in the inversion.
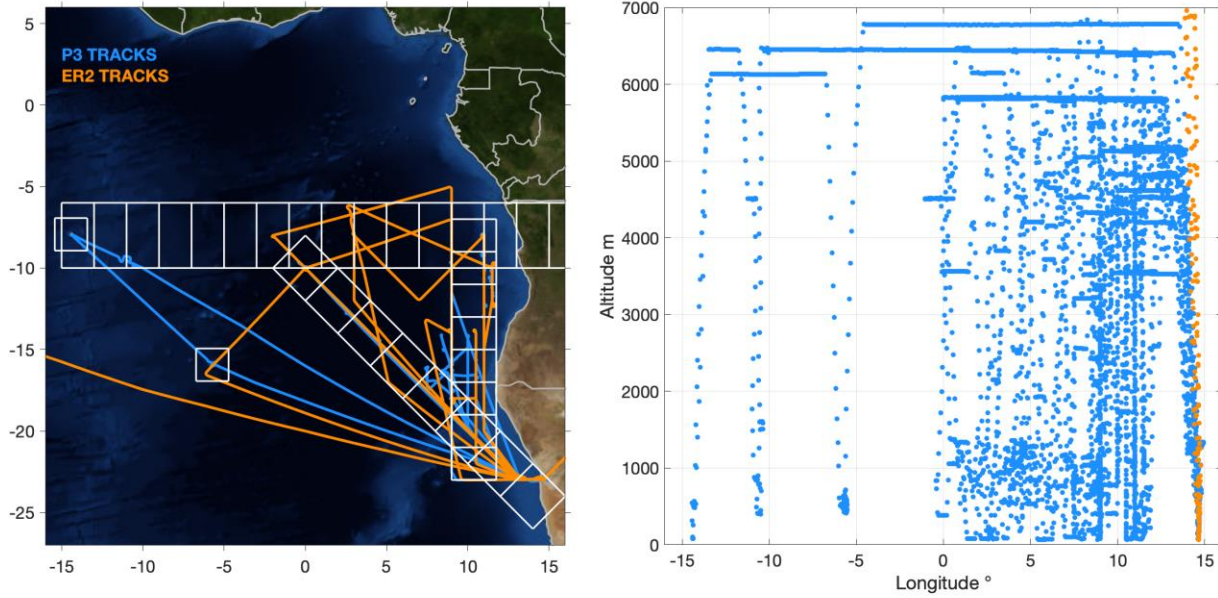
Fig. 3: (left) The boxes selected for the model-observation comparison, overlaid on the P3 and ER2 flight paths (with HSRL-2 observations) from September 2016 and NASA's Blue Marble: Next Generation surface image. (right) The altitude and longitude of the flights averaged over 60s. The ER2 was at altitude of about 20 km except for take-off and landing.
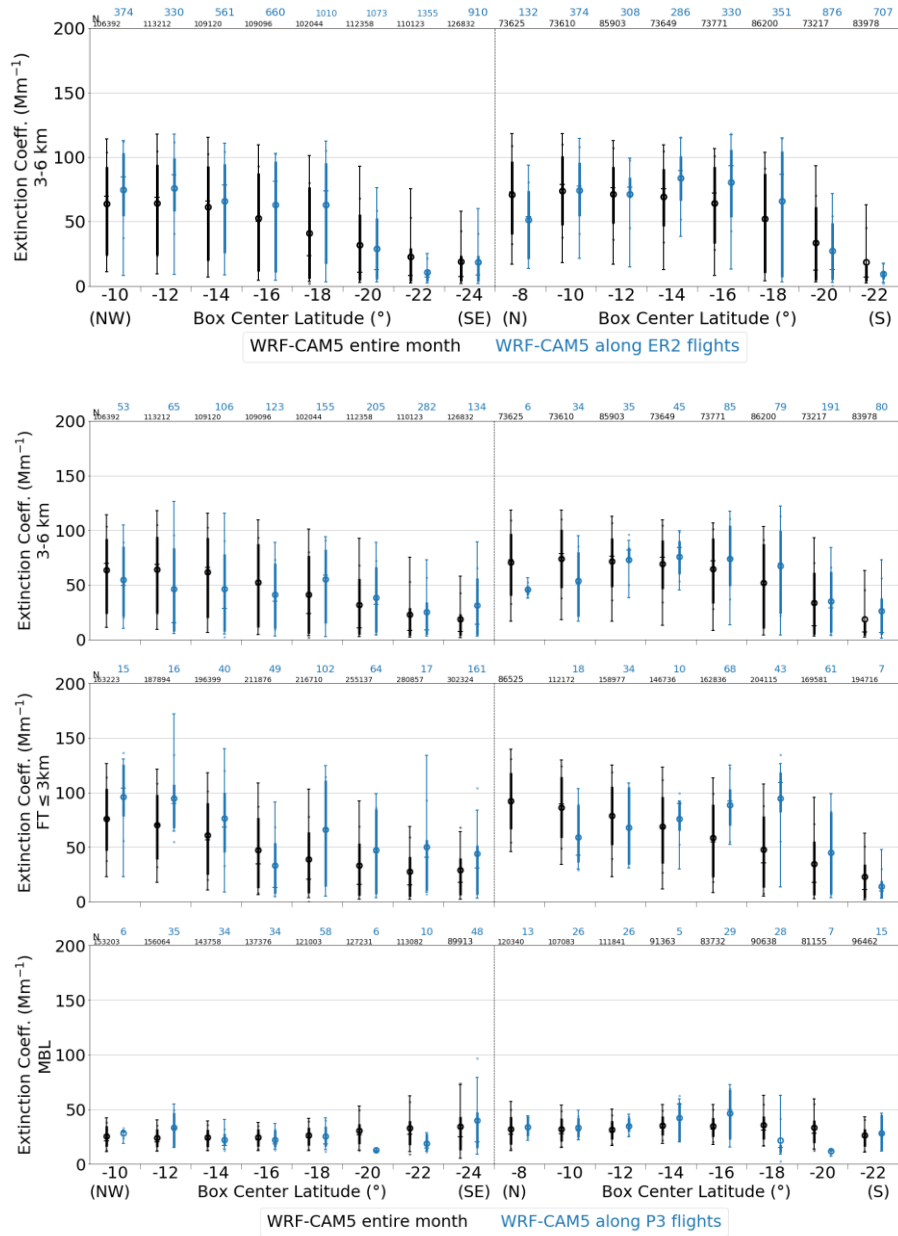
Fig. 4. Extinction coefficients compared between two extracts (monthly climatology and flights) of WRF-CAM5 simulations. The top panel (a) is along the ER2 tracks for altitudes between 3-6 km. The other three panels are for the P3 tracks for 3-6 km (b), the top of MBL to 3 km (c) and the MBL (d). In each panel, the abscissa represents the eight

diagonally aligned boxes and eight meridionally aligned boxes described in Section 3.2 and
Fig. 2. In each box, the bars indicate the monthly climatology (black) and samples along the
flights (blue). Distributions are represented as box-whisker plots encompassing the 10, 25,
50, 75, and 90th percentiles, with circles indicating the mean and mean ± standard
deviation values. The numbers in small print on the top of each panel indicate the number
of samples.
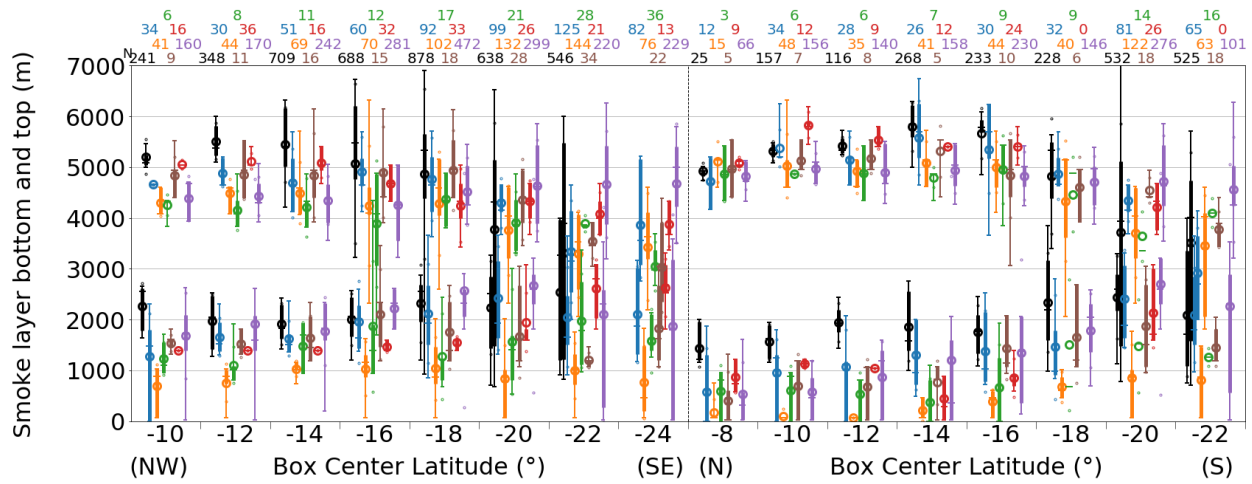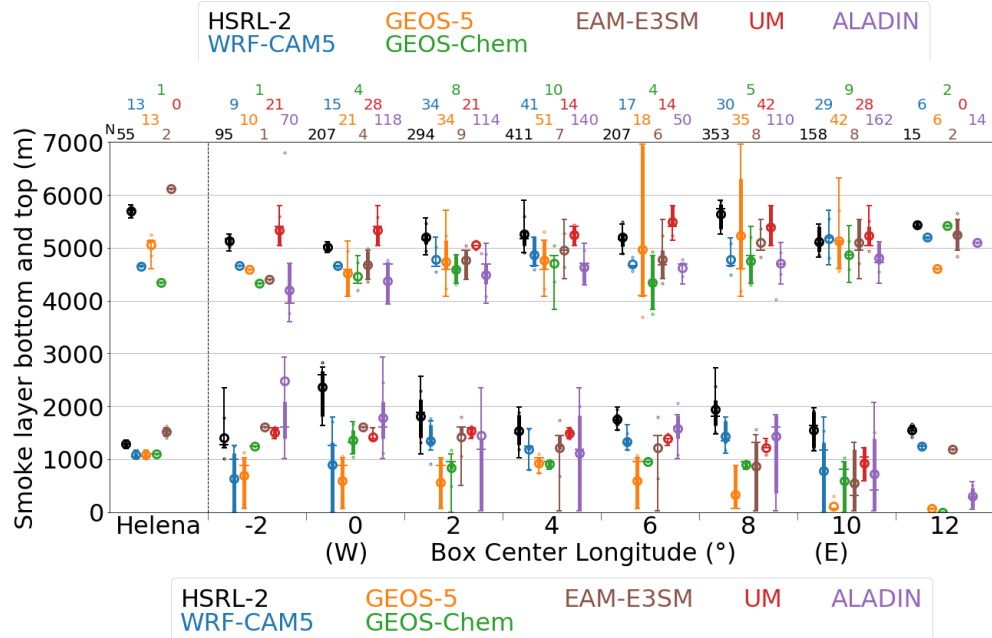
Fig. 5. Smoke layer bottom and top altitudes. Smoke layers are identified through HSRL-2 backscatter intensities exceeding 0.25 Mm^{-1}sr^{-1}, ALADIN extinction coefficient exceeding 17 Mm^{-1} and, for other models, BC mass concentration exceeding 200 ng m^{-3}. See Section 2.1 for details. The top panel (a) is for the diagonal and meridional corridors, while the bottom panel (b) is for the St Helena Island and the zonal corridor. See Section 3.2 and Fig. 2. In each box, the bars indicate the observations from the ER2 aircraft (black) and model

1   **products (colors). See Fig. 4 for a description of each bar and number. The model values**

2   **presented here are sampled along the longitude, latitude and time of the flights. Missing box-**

3   **whiskers indicate products unavailable.**
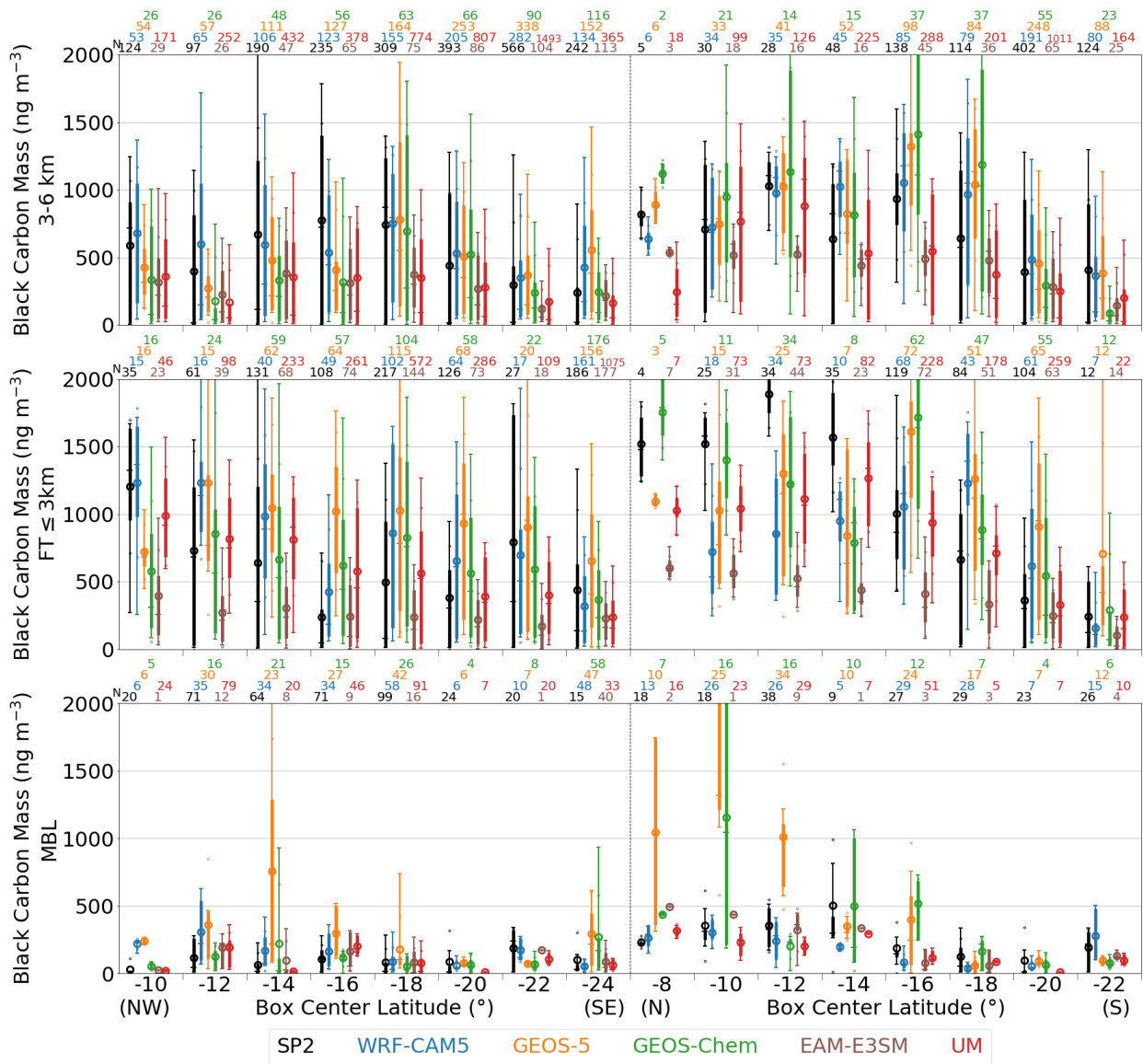
Fig. 6. Black carbon mass concentrations compared between observations (black) and models (colors), for (a) 3-6 km, (b) the top of MBL to 3 km and (c) the MBL. The left-hand side of each panel corresponds to the eight diagonally-aligned boxes of the routine flight path, and the right-hand side to the eight meridionally-aligned ones described in Section 3.2 and Fig. 2. See Fig. 4 for a description of each bar and number.
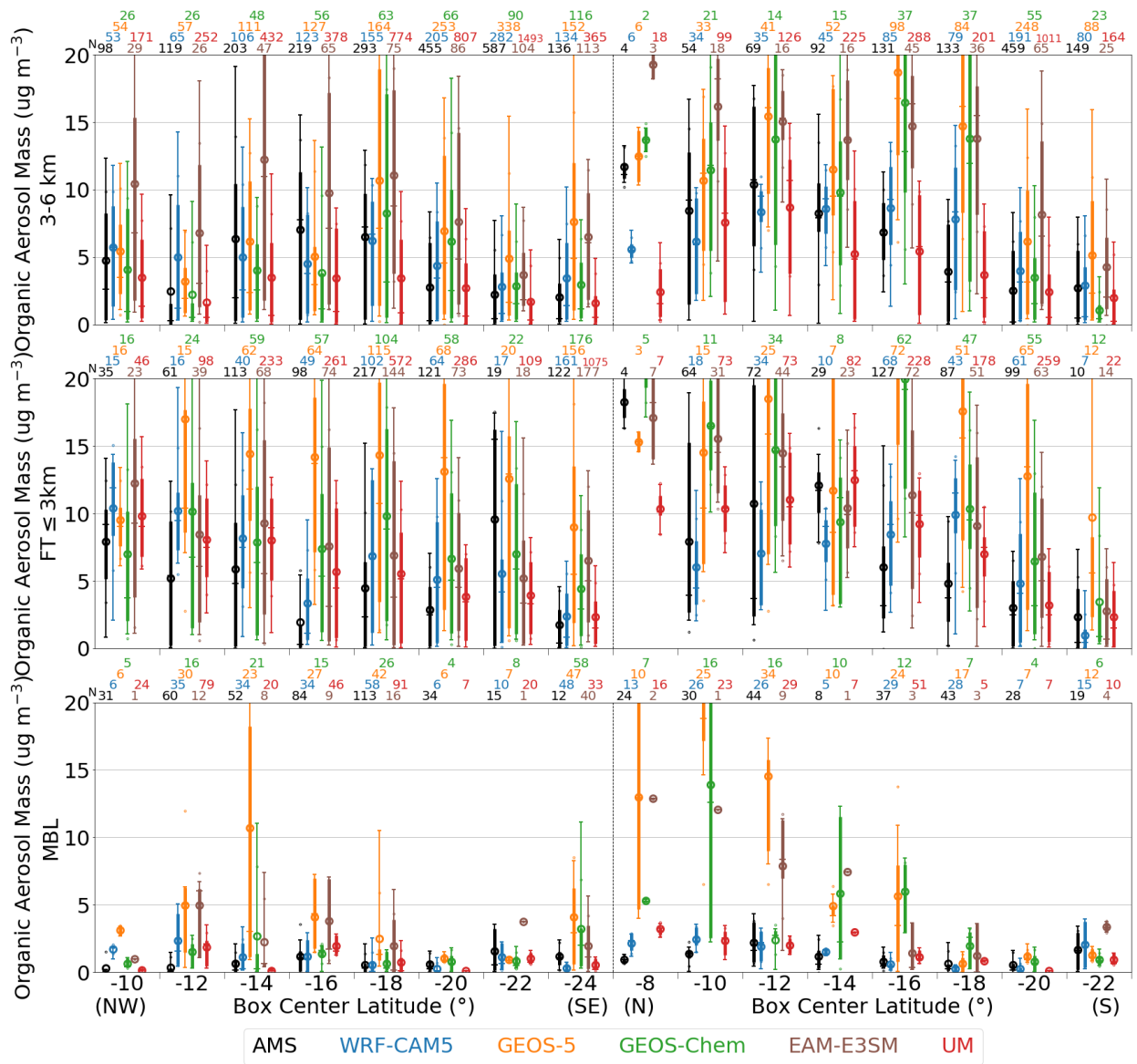
Fig. 7. Same as Fig. 6 but for organic aerosol mass. The range of vertical axis is chosen for clarity. The GEOS-5 mean values in two boxes exceed the range.
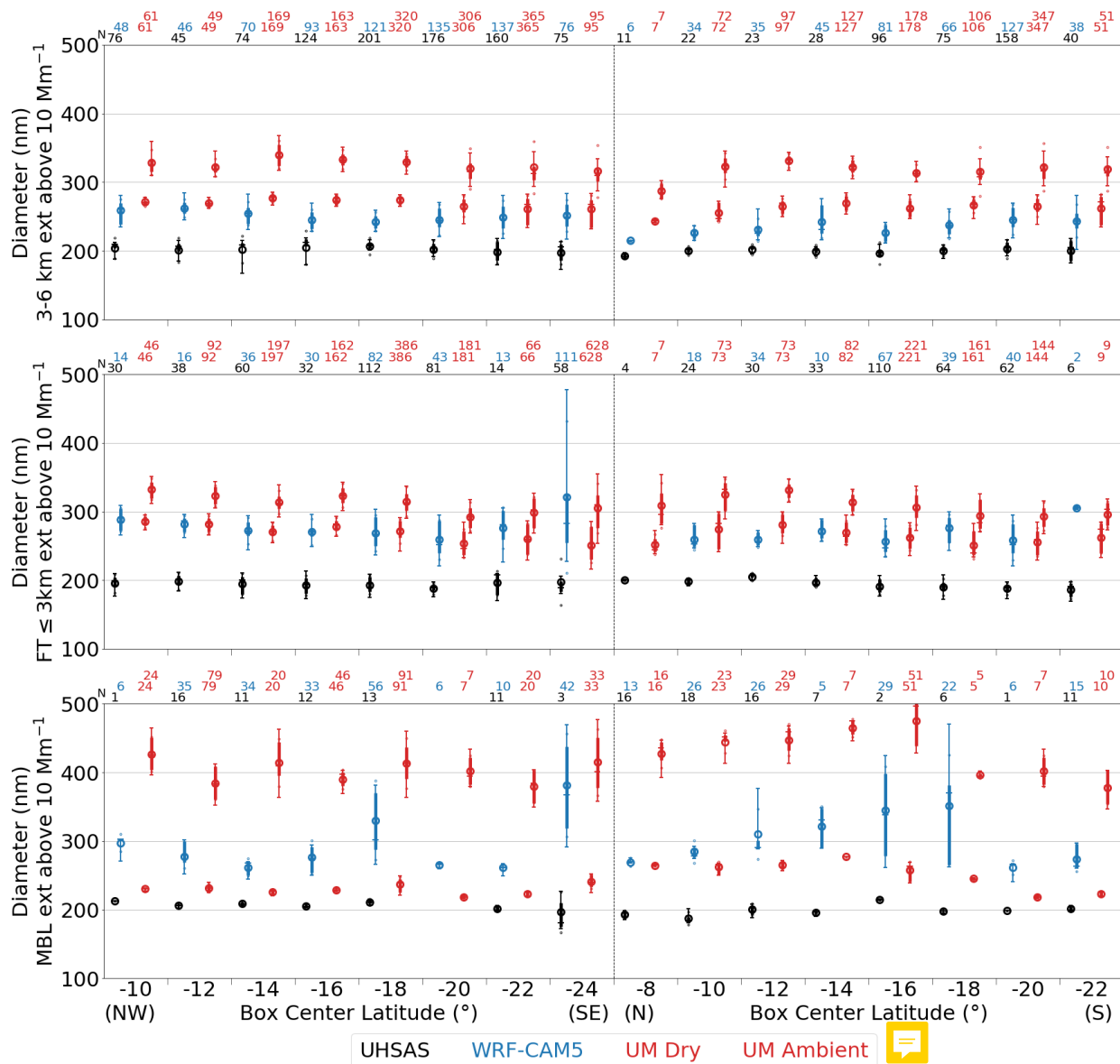
Fig. 8. Same as Fig. 6 but for dry volumetric mean diameter. Samples with 550 nm dry extinctions less than 10 Mm^{-1} are excluded. For UM, the values for ambient RH conditions are given to the right of the ambient ones.
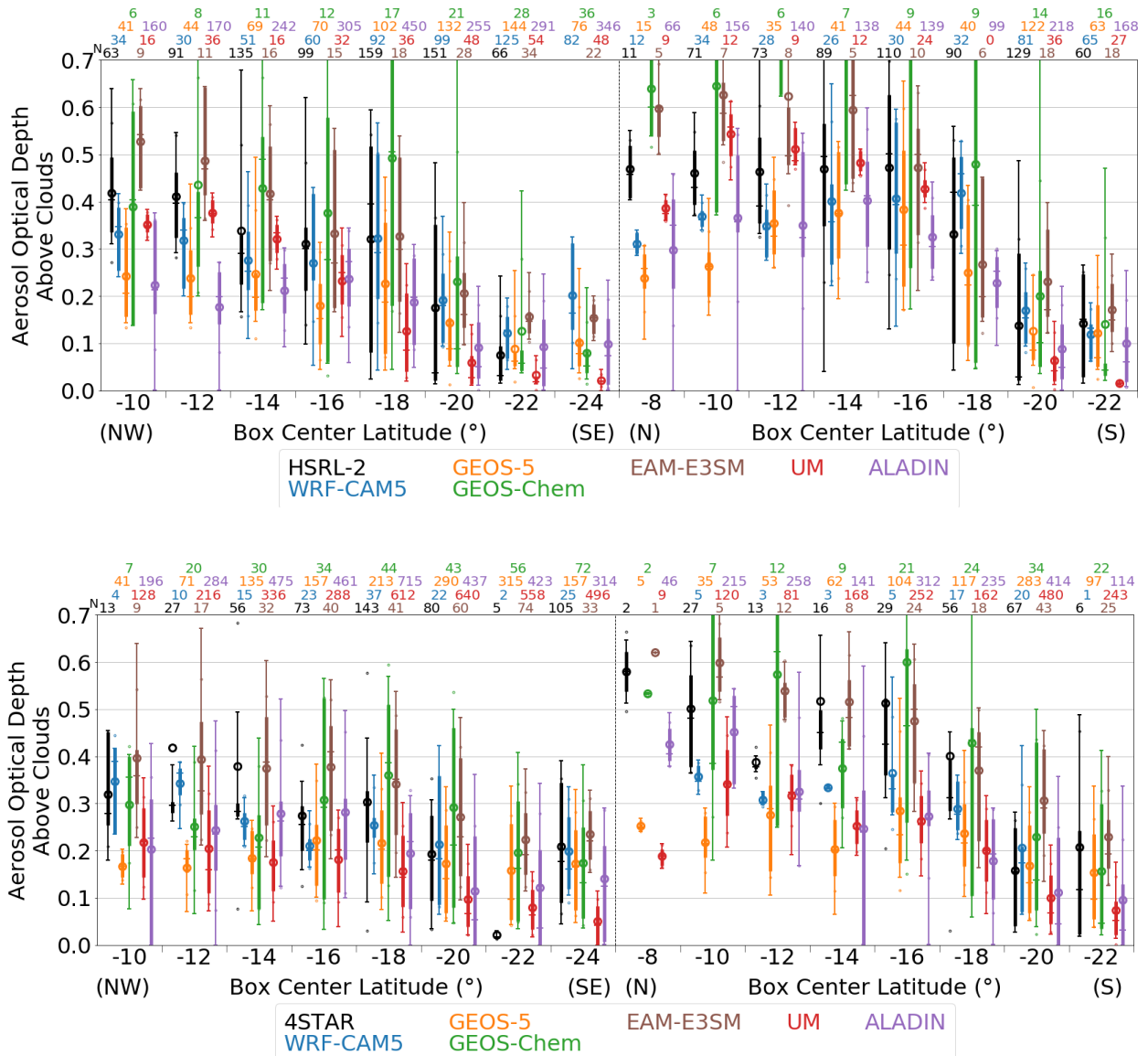
Fig. 9. The aerosol optical depth above clouds (AC-AOD) compared between observations and models. The top panel (a) compares to the HSRL-2 lidar observation from the ER2. The bottom panel (b) compares to the 4STAR measurements made while the P3 aircraft was immediately above clouds.

Neph+PSAP   GEOS-5   EAM-E3SM   UM Dry   UM Ambient
WRF-CAM5   GEOS-Chem
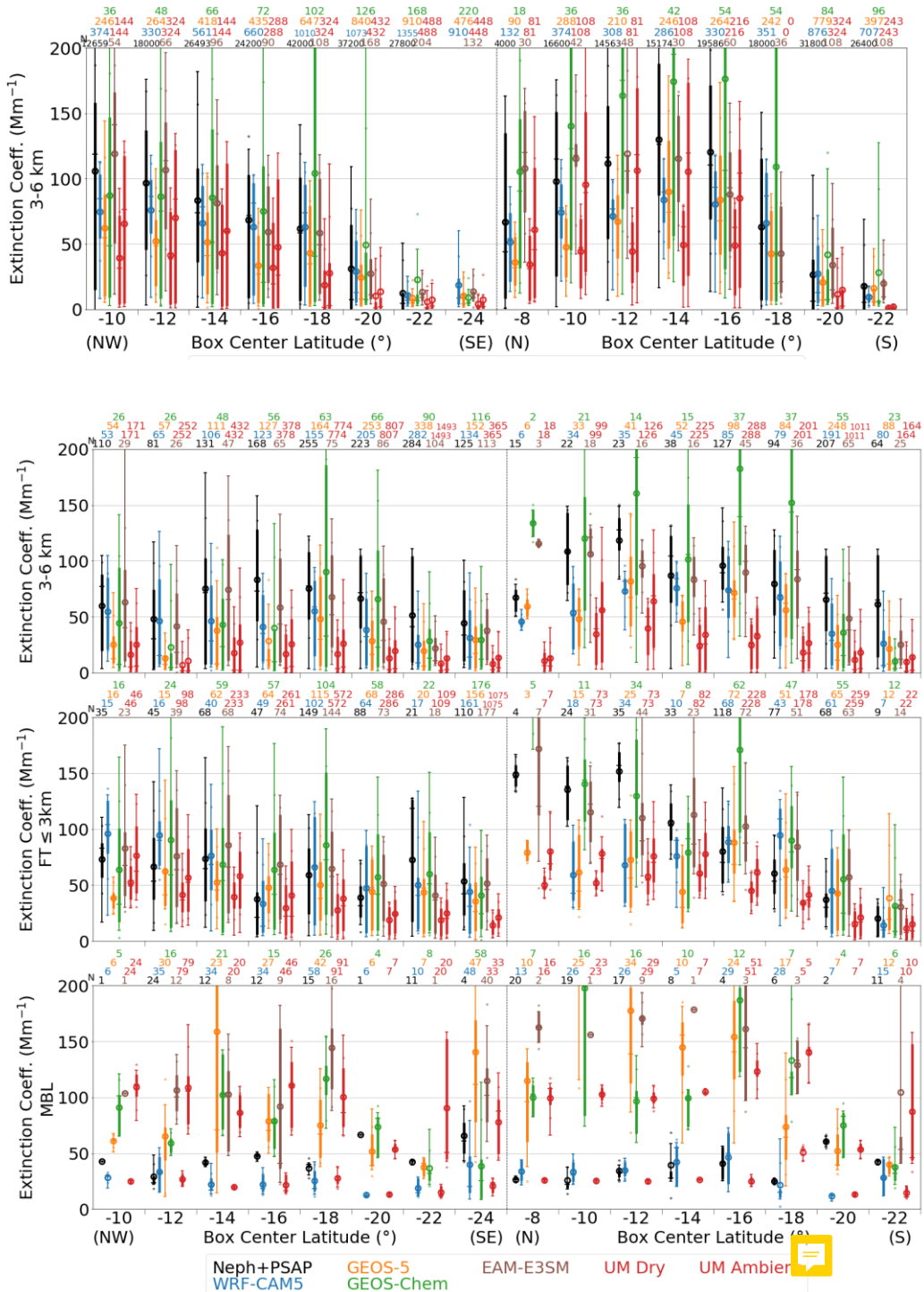
1 Fig. 10. Extinction coefficients compared between observations and models. The top panel
2 (a) compares to the HSRL-2 lidar observation of the ambient particles from the ER2 for 3-
3 6 km. The other three panels compare to the nephelometer and PSAP measurements of
4 dried particles aboard the P3 aircraft for (b) 3-6 km, (c) the top of MBL to 3 km and (d)
5 MBL. For UM, the values for dry RH conditions are given to the left of the ambient ones.
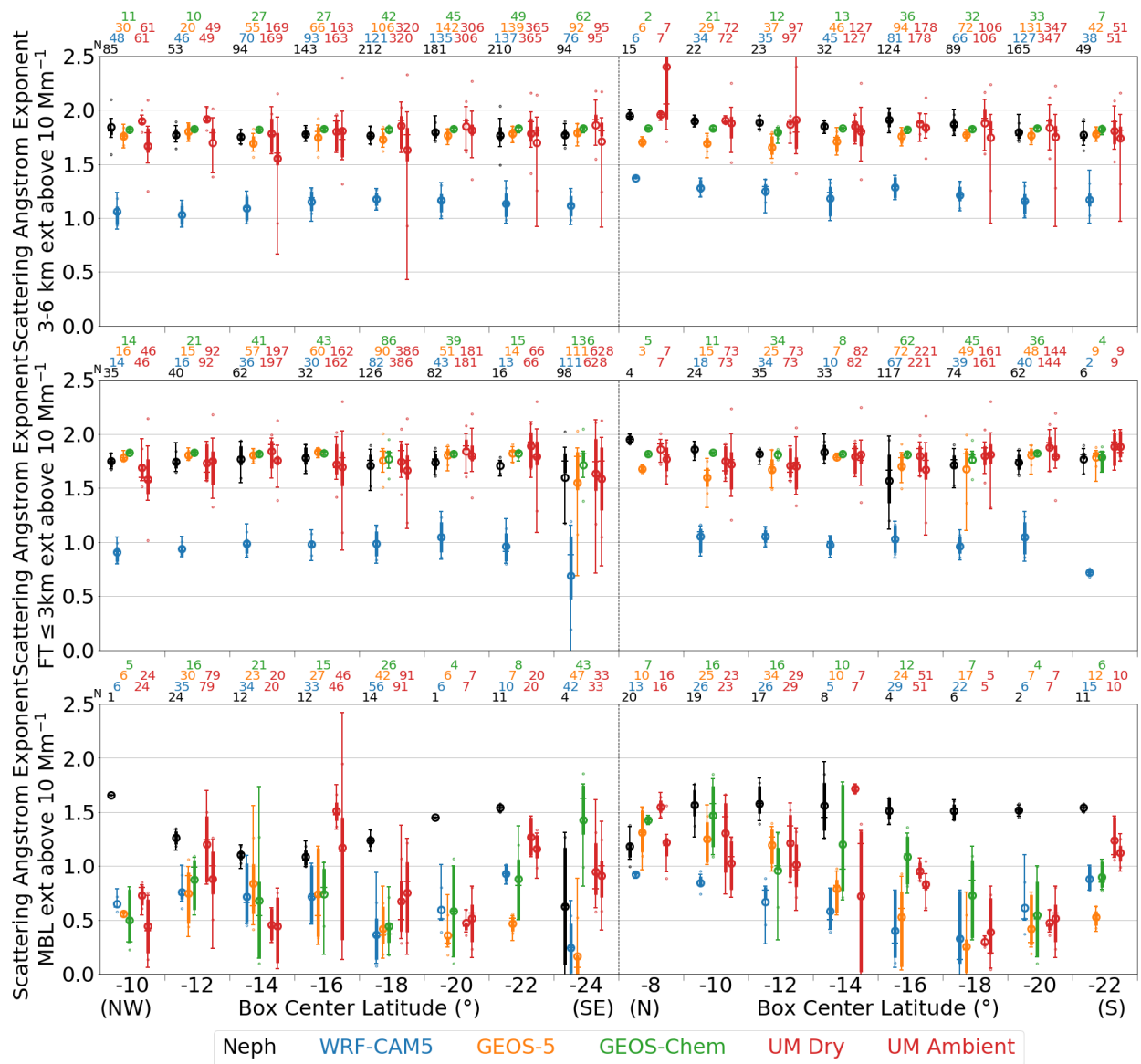
Fig. 11. Same as Fig. 6 but for Scattering Ångström exponent.
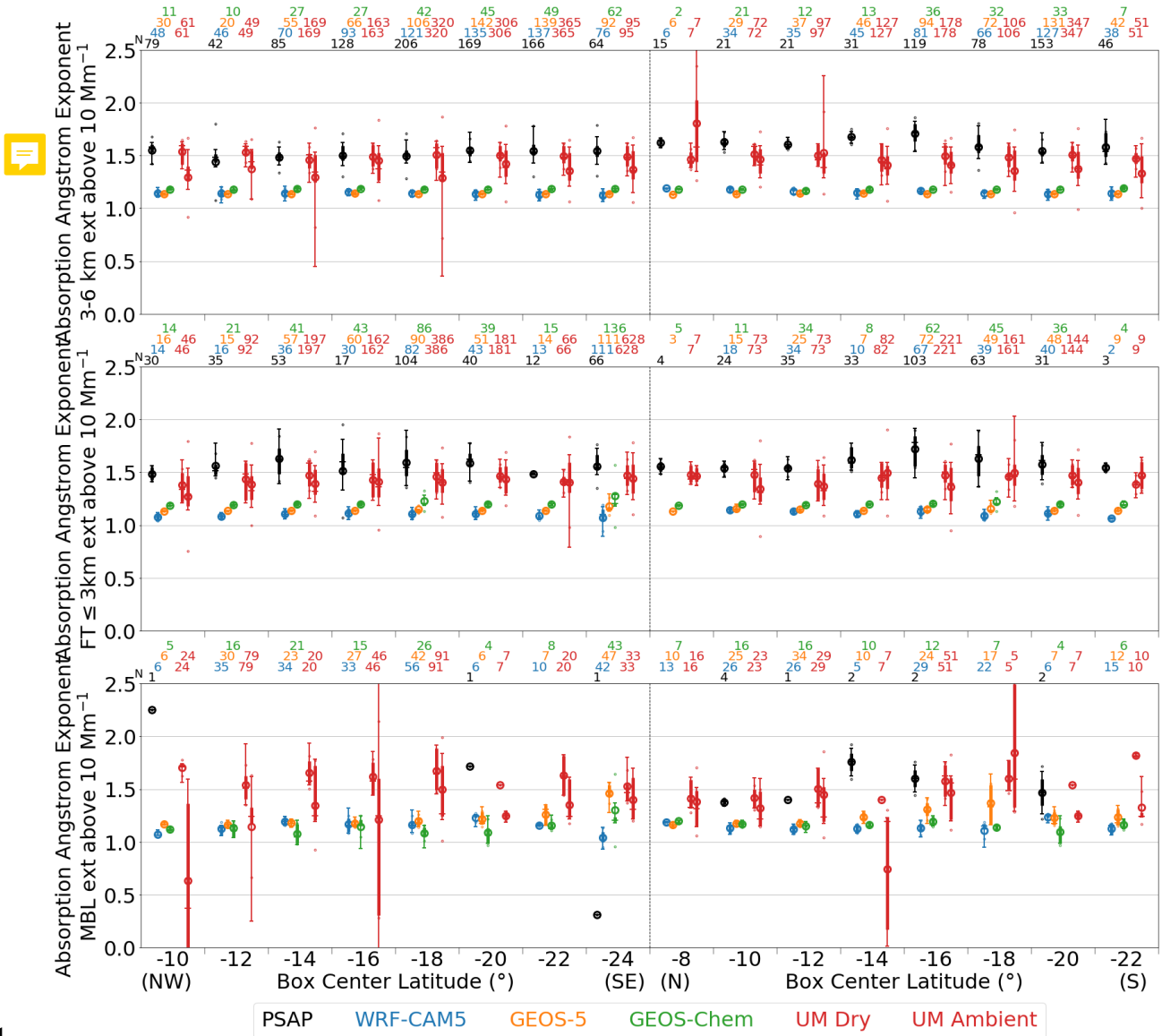
Fig. 12. Same as Fig. 6 but for Absorption Ångström exponent.
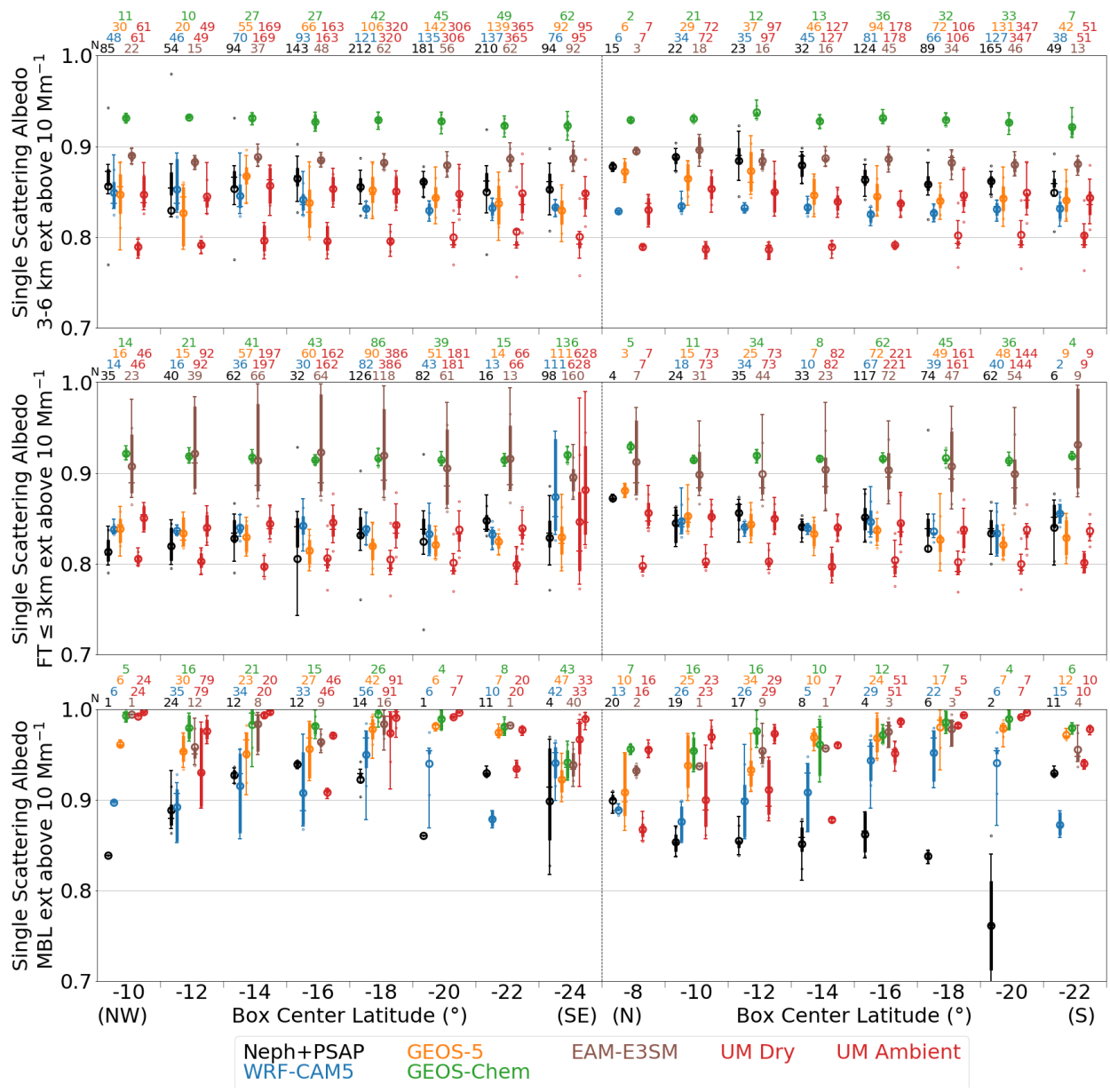
Fig. 13. Same as Fig. 6 but for SSA.
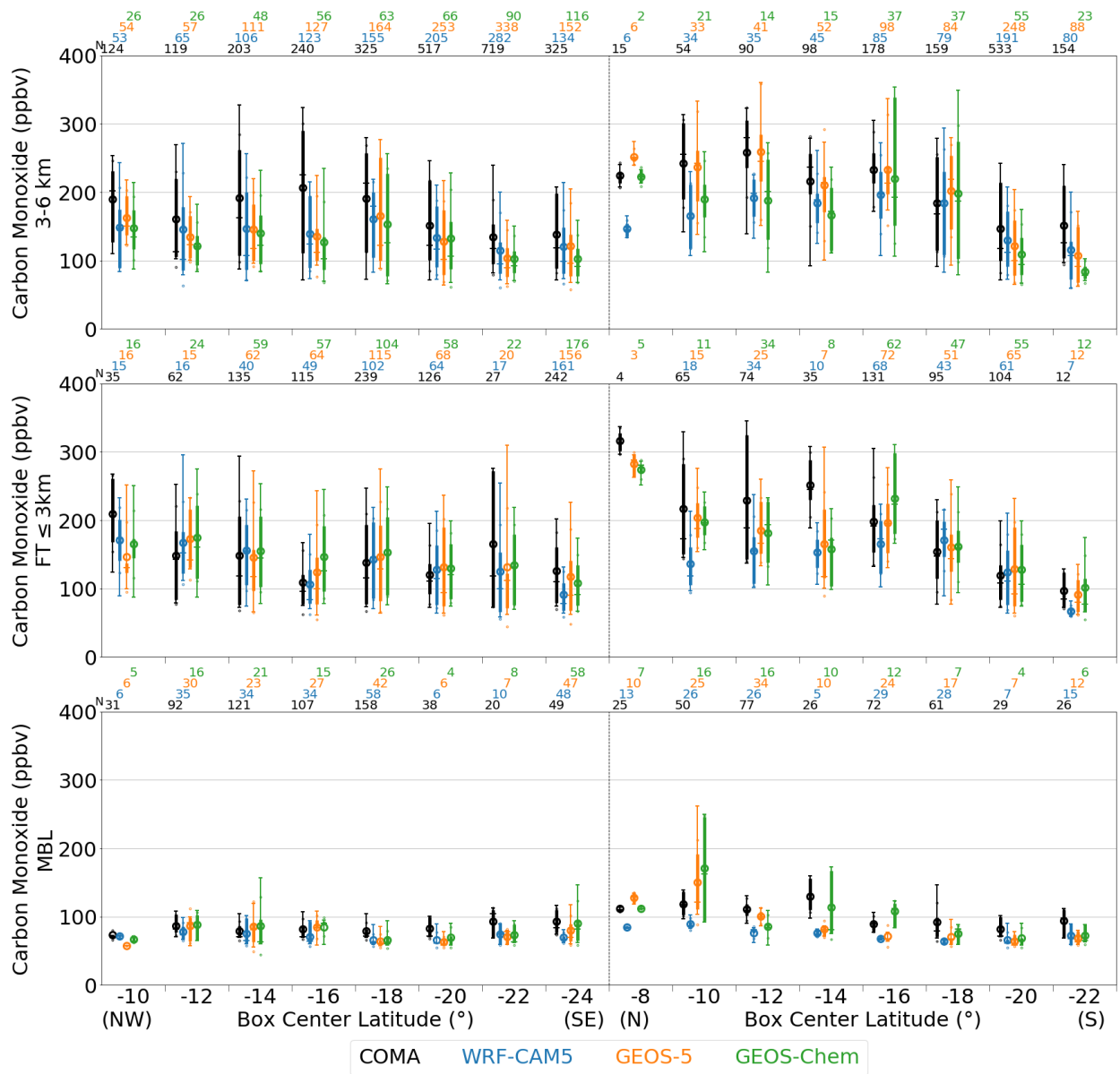
2   **Fig. 14. Same as Fig. 6 but for carbon monoxide mixing ratio.**
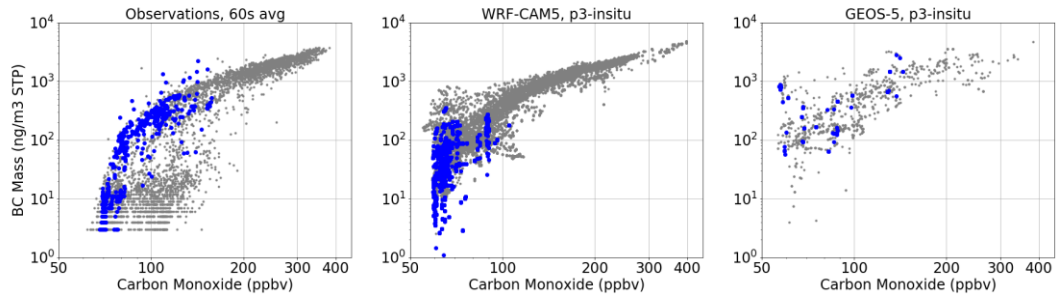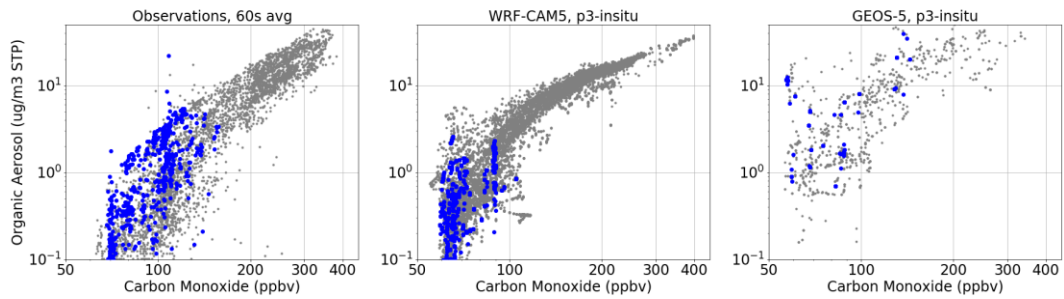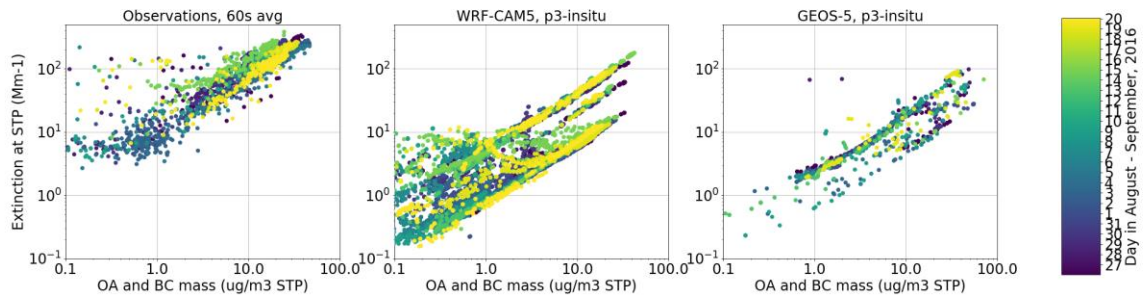
Fig. 15. (a) Black carbon mass per air at 1013.25 hPa, 273.15 K compared with carbon monoxide mixing ratio on a 60s average basis for the observation in the FT (grey) and boundary layer (blue). (b, c) Same variables but from the WRF-CAM5 and GEOS-5 models, respectively, sampled along the P3 flight tracks. (d, e, f) Same as the first row but with organic aerosol mass in place of BC mass. (g, h, i) The mid-visible light extinction by dried particles compared with the sum of OA and BC masses, for the FT only. The color indicates the day of measurements.
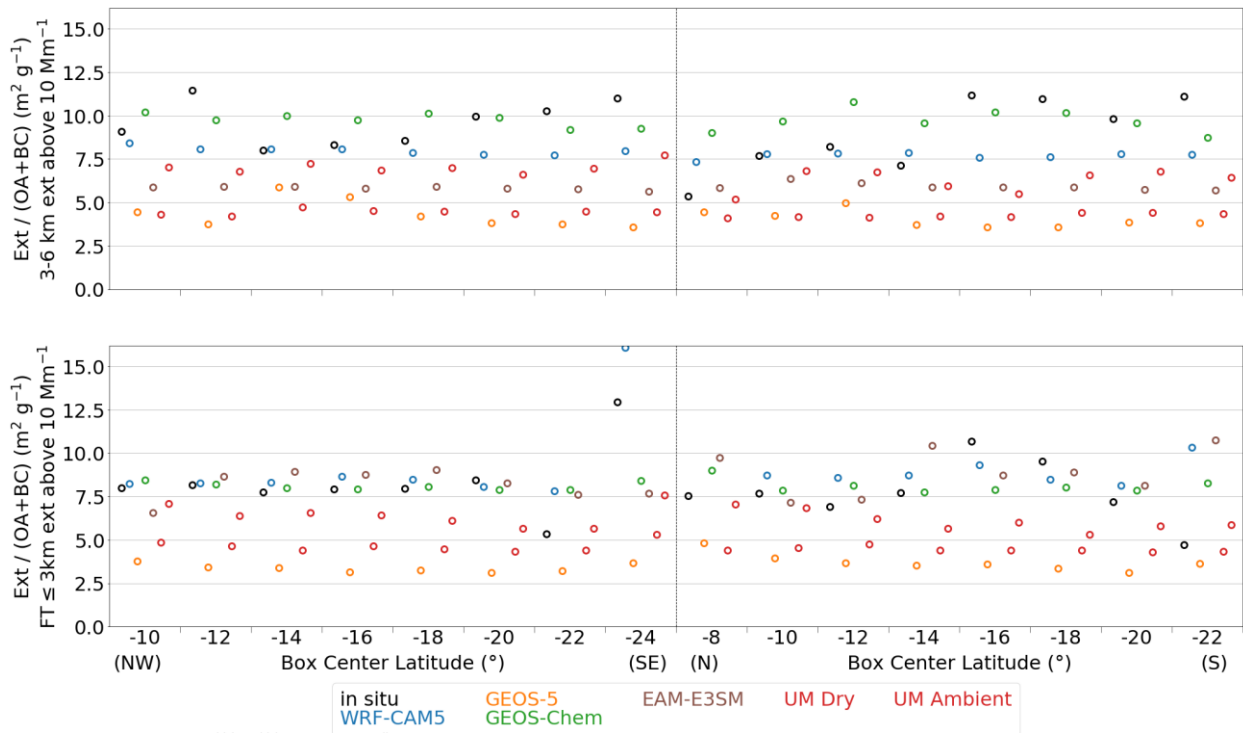
2   **Fig. 16. The ratio of extinction to the sum of organic aerosol and black carbon masses,**
3   **computed for box mean values. The in situ observation of extinction is for dried particles,**
4   **while the models refer to ambient humidity conditions except for UM Dry. The top and**
5   **bottom panels are for 3-6 km and for the top of boundary layer to 3 km, respectively.**